Encyclopedia of
Atmospheric Sciences

Editor-in-Chief
James R. Holton
University of Washington, Seattle, U.S.A.
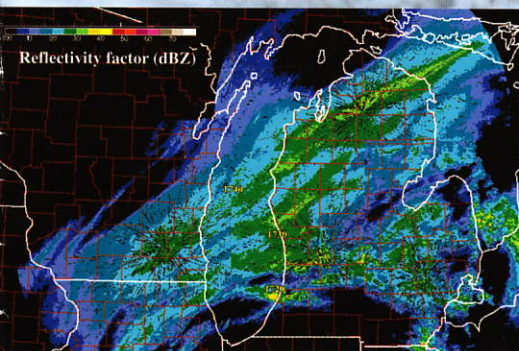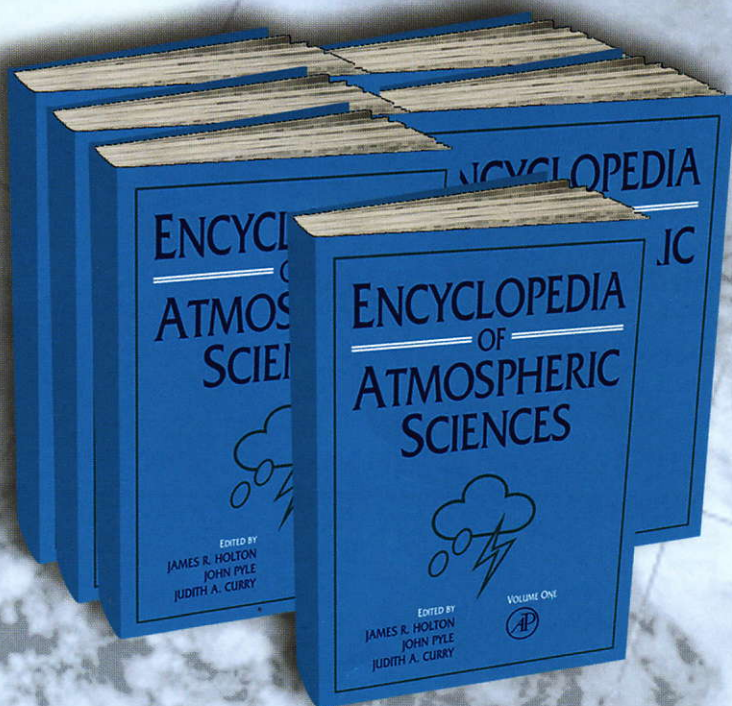
Editors
John Pyle
University of Cambridge, U.K.

Judith A. Curry
Georgia Institute of Technology, U.S.A.

Reflectivity factor (dBZ)

"I greatly welcome this unique Encyclopedia of six volumes containing 340 contributions, each of approximately 4000 words, on all major aspects of atmospheric science and cognate subjects such as oceanography and hydrology, and that range from Acid Rain to the World Climate Research Programme. ... The six volumes promise to be the most comprehensive and widely consulted publication in the atmospheric sciences for years to come. Every scientist engaged in post-graduate teaching and research in the subject will need access to a copy."

**—From the Foreword by Sir John Mason, F.R.S.,
Imperial College, London, U.K.**

www.academicpress.com/atmospheric

ACADEMIC PRESS
An imprint of Elsevier Science

TELECONNECTIONS

S Nigam, University of Maryland, MD, USA

Introduction

The term teleconnection is often used in atmospheric sciences to describe the climate links between geographically separated regions. The remote region need not exhibit fluctuations of the same sign in order to be 'teleconnected'. In fact, the interesting teleconnections often involve contemporaneous variations of opposite signs. Climate analysis is facilitated by the construction of a teleconnection map, which describes the linkage between a region of interest (a base point) and all other points in the domain that are farther than the de-correlation length scale of the variable. Teleconnection maps thus provide information about the structure of recurrent climate variability that is characterized by the correlation-at-a-distance feature. The maps are useful because climate variability often manifests itself with such structure: For example, winter variations in temperature and rainfall over southern Europe and the Iberian peninsula are frequently opposite to those over northwestern Europe and Scandinavia.

Teleconnection maps were first constructed for meteorological parameters measured at the Earth's surface, such as the atmospheric pressure. The selection of the base point is a critical first step, and was historically guided by the investigator's insights and interests. Today, base points can be selected more objectively, and the robustness of teleconnection maps can be ascertained by independent analysis. The statistical correlation of the fluctuations provides a measure of the teleconnection strength. The structure and strength of the teleconnection patterns change with season, altitude, choice of variable, and even temporal averaging of data. There are interesting differences between the hemispheres too, in part due to the more zonal nature of the Southern Hemisphere circulation. Teleconnectivity in the Northern winter circulation has been extensively analyzed, and teleconnection patterns are well established only for this season.

Climate teleconnections are constructed from observations that have been averaged in time over a period that is long enough to suppress the day-to-day weather fluctuations, but short enough to retain the seasonal-to-interannual component of climate variability. Monthly averages have typically been used since a month is longer than the period of most large-scale synoptic waves in the troposphere. Climate teleconnections thus highlight the "standing" component of low-frequency variability – one with geographically fixed nodes and anti-nodes. The connectivity of remote regions manifest in the teleconnection maps indicates the potential significance of remote forcing in the generation of regional climate anomalies. A teleconnection map based on contemporaneous correlations however cannot, by itself, discriminate between the forcing and response regions.

Although the structure of the prominent teleconnection patterns has been known for sometime, the reasons for their origin are not yet well understood. For example, the mechanisms that excite and sustain the North Atlantic Oscillation (NAO) – one of the notable and earliest discovered patterns – are still being actively investigated. In the context of such investigations, it has been questioned if the teleconnection patterns which are, typically, regional (e.g., NAO) robustly portray the spatial structure of variability from the viewpoint of elucidation of the underlying processes and interactions.

Such concerns are relevant since the canonical teleconnection patterns typically represent the mature phase of variability. The mature-phase patterns, however, need not resemble the nascent-phase structure, which may be more revealing of the excitation mechanism. Identification of the evolution process from analysis of the mature-phase structure is thus difficult. The spatial imprint of variability captured by a teleconnection pattern can also be ineffective in revealing the underlying mechanisms if the region in question is the locus of two temporally independent physical and/or dynamical processes. While cautionary, these remarks do not call for a radically new analysis paradigm. Instead, they point to the need for more comprehensive analysis of variability, particularly in the spatiotemporal domain, to facilitate insights into the evolutionary process.

Analysis Method

Teleconnection patterns can be extracted from correlation analysis and from the calculation of principal components, among other techniques. Both methods have been widely used in climate research, and each offers some advantages.

Correlation

Correlation analysis is the more straightforward of the two methods. Consider a meteorological field such as geopotential height which denotes the height of an isobaric surface in the atmosphere. Geopotential height, ϕ, is a function of longitude and latitude, and assume that it is defined at M grid points; ϕ_i represents height at the ith longitude–latitude grid point. Geopotential height is also a function of time, and its monthly mean value is assumed to be available for several winters (N winter months). Interest in the variability of climate leads to the consideration of departures of monthly mean heights from their calendar month climatologies, with the prime denoting the departures; $\phi'_{i,k}$ represents the height departure at the ith grid point in the kth month. The correlation in height departures at two grid points, i and j, is denoted by $\mathbf{H}_{ij}$, and defined as

$$\mathbf{H}_{ij} = \frac{\sum_{k=1}^{N} \phi'_{i,k}\phi'_{j,k}}{\left(\sum_{k=1}^{N} \phi'^2_{i,k}\right)^{1/2}\left(\sum_{k=1}^{N} \phi'^2_{j,k}\right)^{1/2}}$$

Knowledge of the correlation matrix, $\mathbf{H}$, can be used to construct a teleconnectivity map (T_i) which objectively identifies the base points associated with various teleconnection patterns. The map is constructed by associating the *magnitude* of the strongest negative correlation between a grid point and all others with that grid point, i.e., $T_i = |$ most negative member in the ith row of the correlation matrix $\mathbf{H}_{ij}|$. The local maxima in this map identify potential base points. Linkage between the neighboring base points can be ascertained by examining the sites of their strongest negative correlations. A cluster of linked base points constitutes the core of the teleconnection pattern, and many of the prominent patterns can be identified using this technique.

Teleconnection Map

Climate teleconnections were first investigated in the sea-level pressure field. Sea-level pressure is however an ill-defined quantity over land, particularly near the mountains; it can moreover be influenced by local meteorological processes. Teleconnectivity is thus better probed in upper-air data, which became available since the mid-to-late 1940 s. The preferred analysis variable in recent decades has been the geopotential height – a measured quantity whose horizontal and vertical gradients are proportional to the wind and temperature, respectively. The Northern winter is the focus of attention here since teleconnection patterns have been identified with some certainty for only this season.

Figure 1 shows the teleconnectivity in Northern winter height fluctuations at the 500 hPa level. The map is constructed from correlation analysis of the December, January, and February height anomalies. The analysis period (1962/63–1976/77 winters) and domain (20–90°N) are chosen to follow closely the pioneering study of Wallace and Gutzler which introduced this objective method for identifying teleconnections. The only difference between that study and the present one is in the slight differences between the analyzed data sets. Since the operationally produced (theirs) and retrospectively analyzed (ours) data sets differ primarily in their representation of divergent circulation, the height field – a rotational component – is expected to be minimally different in the two data versions. Not surprisingly, **Figure 1** is a close reproduction of the teleconnection map shown in **Figure 7B** of Wallace and Gutzler.

Four base points exhibiting equally strong negative correlations with remote regions are identified over the Pacific in the above analysis: the two in the eastern Pacific – one southward of the Aleutian and the other westward of Hawaiian Islands – are linked to the local maxima over north-western Canada and south-eastern
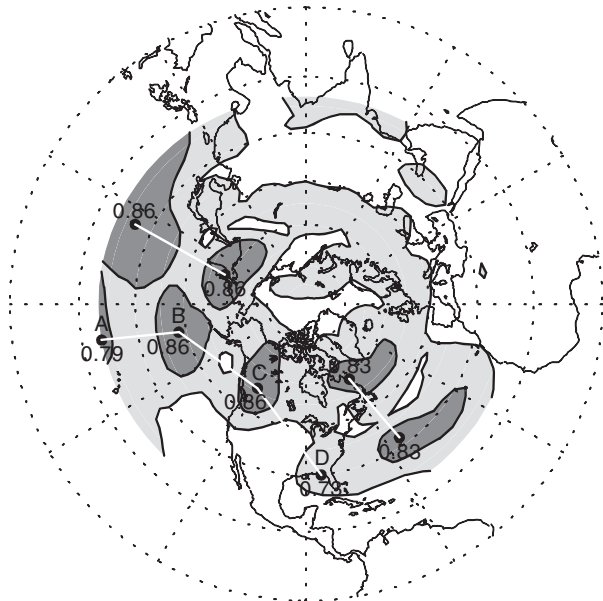
Figure 1 Teleconnectivity in geopotential height fluctuations of the 500 hPa pressure surface. Monthly fluctuations poleward of 20° N are analyzed in Northern winter (December, January, and February) during December 1962–February 1977. The teleconnection map is produced by plotting the magnitude of the strongest negative correlation between a grid point and all other points at the 'base' point. The correlation magnitude is contoured with an interval of 0.15, and only values greater than 0.6 are contoured. Light and dark shading represents values above 0.6 and 0.75, respectively. Values at the local maxima are shown. White lines connect the geographical regions that are 'teleconnected'. Points A–D define the Pacific/North American pattern of variability.

United States, and the four centers together define a spatially extended and prominent teleconnection called the Pacific/North American (PNA) pattern. In contrast, the two centers in the western Pacific – one over the Kamchatka peninsula and the other extending longitudinally in the subtropics – define a more regional pattern, called the Western Pacific pattern. This meridionally dipolar, mid-tropospheric height pattern is associated with fluctuations in the position of the Asian-Pacific jet, and linked at the surface to a long known pattern in sea-level pressure variability, the North Pacific Oscillation. An Atlantic counterpart is also evident in **Figure 1**: a meridional dipole in mid-tropospheric height variability between the subtropics and higher latitudes, which is also associated with a well-known pattern of sea-level pressure variability, the NAO.

Correlation analysis can yield the structure of teleconnection patterns, but does not provide information on temporal variability of their amplitude. An index for amplitude variations can however be constructed using the magnitude of fluctuations at the base points. Since the base points constituting a given pattern do not all produce comparable anticorrelated remote responses, their contributions to the pattern index need not be equally weighted, although this option is exercised here in the interest of comparison with earlier studies. The PNA index is thus defined as

$$\alpha_{\text{PNA}}(k) = \frac{1}{4}\left(\frac{\phi'_{\text{A},k}}{S_\text{A}} - \frac{\phi'_{\text{B},k}}{S_\text{B}} + \frac{\phi'_{\text{C},k}}{S_\text{C}} - \frac{\phi'_{\text{D},k}}{S_\text{D}}\right)$$

where A, B, C, and D are the marked base points of the PNA pattern (**Figure 1**). The contribution of every other base point is negatively weighted in the index definition since the base points are anticorrelated with their immediate neighbors. S_i in the above definition denotes the standard deviation of height anomalies at the ith longitude–latitude grid point, i.e.,

$$S_i = \left(\frac{1}{N}\sum_{k=1}^{N} \phi'_{i,k}\phi'_{i,k}\right)^{1/2}$$

PNA pattern of variability The variability associated with the PNA teleconnection pattern is shown in **Figure 2**. The PNA index (α_{PNA}) is shown in panel D, while its regression on the 500 hPa height and sea-level pressure fields are shown in panels A and B. The PNA teleconnection is associated with robust height anomalies over Northern Pacific and Northwestern Canada. In the positive phase, geopotential height is lower over the North Pacific, implying the presence of anomalous westerlies over the midlatitude Pacific, from geostrophic balance. This is tantamount to an anomalous eastward extension of the climatological Asian-Pacific jet. The sea-level pressure anomalies (panel B) are impressive over the North Pacific where a deep trough (>7 hPa) is centered just south of the Aleutians, but the anomalies over land are more modest. In both cases though, the anomalies are in phase with the 500 hPa height features, pointing to the vertically coherent structure of PNA variability in the troposphere.

The pattern's linkage with sea surface temperature (SST) is shown in panel C. As the signal extends into the Tropics where the variance of SST is stronger, correlations are shown instead of regressions in order to convey the significance of the PNA linked SST anomalies. The PNA pattern is evidently linked more strongly to SST variability in the extratropical Pacific basin, where correlations reach 0.6. The absence of strong linkage with tropical Pacific SSTs, along with temporal variations of the PNA index, particularly the changes in sign within a winter season in several of the years, indicates that PNA variability is not related to El Niño Southern Oscillation (ENSO) variability. In the analyzed 15 years, ENSO variability was strong during 1966 and 1973 (El Niño winters) and 1971, 1974, and 1976 (La Niña winters). Inspection of **Figure 2D** however shows the index variations to be unremarkable in these years, further indicating that PNA and ENSO variabilities are unrelated, at least in their mature phases.

The presence of significant SST correlations in the Pacific basin raises the issue of air–sea interaction: are SST anomalies in the eastern midlatitude Pacific, specially along the US and Canadian west coasts, produced by atmospheric forcing or by processes internal to the ocean? The question is investigated later from analysis of lead/lag relationships between atmospheric and oceanic fields, but some insight can be obtained from the structure of contemporaneous variability and knowledge of climatology. For instance, the longitudinal collocation of the sea-level pressure trough and cold SSTs (**Figure 2**) suggests that SST cooling can result from the impact of strengthened westerlies on heat fluxes and vertical mixing at the ocean surface. The counterclockwise circulation, which strengthened surface westerlies on the equatorward flank of the trough, also strengthens the southerlies (i.e., coming from the south) over the far eastern basin. These winds can generate strong downwelling in the coastal zone, and shield the upper layers from the influence of cold subsurface water. Thus, SST warming along the North American coast (**Figure 2C**) can also be produced by atmospheric forcing. While plausible, these ideas need to be corroborated from a more careful analysis of the evolution of PNA variability, which is pursued later.
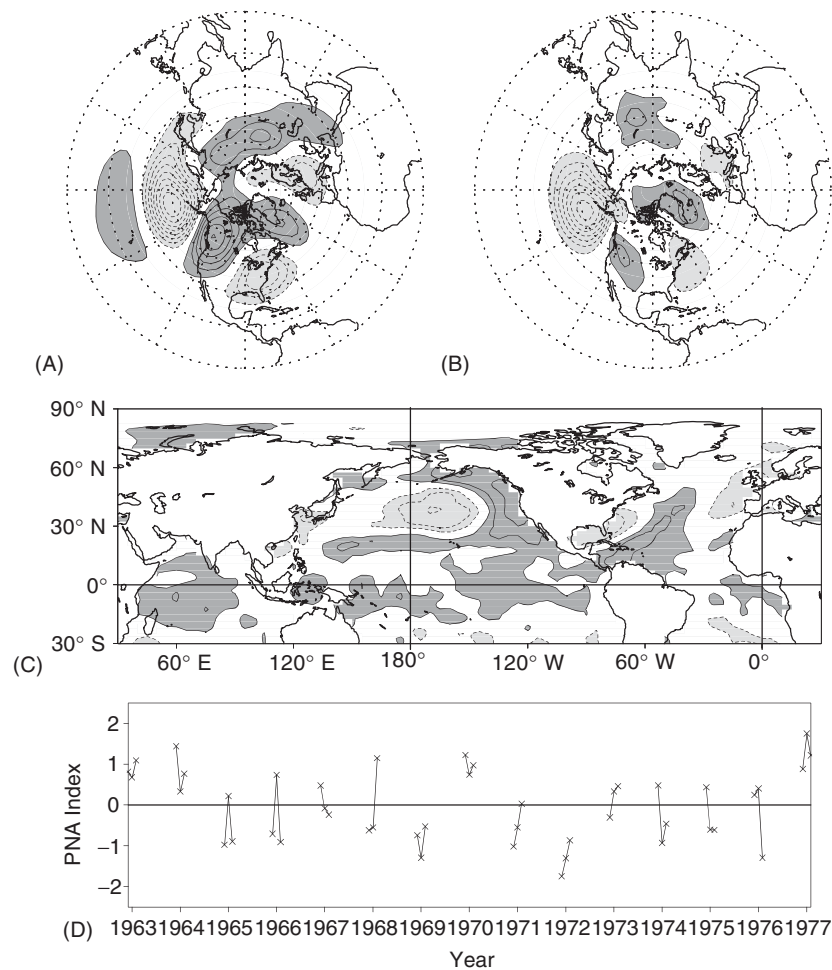
Figure 2 Variability associated with the Pacific/North American teleconnection pattern during 1962/63–1976/77 winters: (A) 500 hPa height anomalies contoured in 10 m intervals, (B) sea-level pressure anomalies with a 1.0 hPa interval, (C) sea surface temperature correlations with a 0.2 interval, and (D) the monthly PNA index (for definition, see text) used in obtaining the regressed (or correlated) variability. The dark (light) shading in panels A–C denotes positive (negative) values in excess of the contouring interval. The zero contour is suppressed in the top three panels.

Stability of the teleconnections The map shown in **Figure 1** identifies the prominent teleconnections in winter height fluctuations in the Northern extratropics. Interestingly, the characteristic mid-tropospheric height pattern associated with ENSO variability is not one of them. Since this pattern is not very strong, and because it spans the PNA region – the home of a number of leading teleconnection patterns – its identification from correlation analysis is, evidently, challenging. Is this because height fluctuations in the Tropics were not simultaneously analyzed in investigation of teleconnectivity? The issue is examined by repeating the teleconnection analysis, but this time in an expanded meridional domain (0–90° N) and period (1958–98). Fluctuations in the Northern Tropics are included to see if this leads to identification of the ENSO-related height pattern. The expanded analysis period, covering 40 winters, on the other hand, will

allow an assessment of the stability of the teleconnection patterns. Results from the new analysis are displayed in **Figure 3**. Except for some movement of the base points, the major teleconnections are all present in the new analysis. The PNA teleconnection has lost the base point near Florida, and its Pacific Northwest center is now somewhat eastward of its earlier position. The NAO pattern is less perturbed, with only a 10–15° eastward shift in its subtropical center. It is noteworthy that despite the inclusion of tropical fluctuations in the analysis, the ENSO-related height pattern remains unidentified.

The 500 hPa height anomaly associated with PNA variability in the extended period analysis is shown in **Figure 4A**. It is obtained, as before, by regression, except that the PNA index in the new analysis is constructed from height data at only three base points (A–C in **Figure 3**). Notwithstanding this difference,

(A)
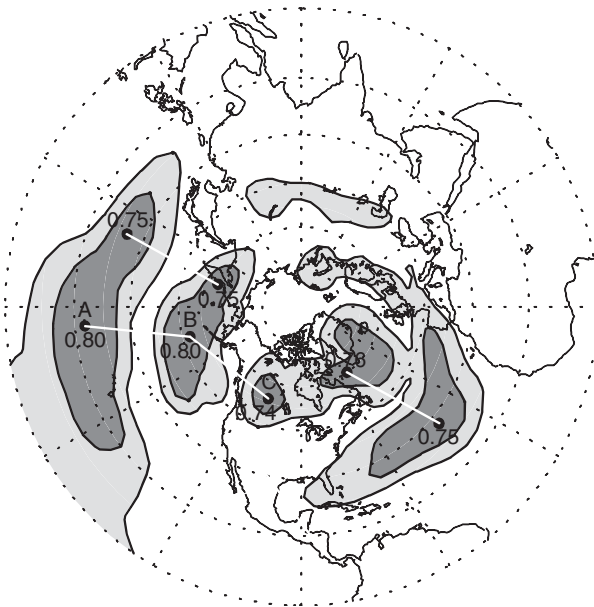
Figure 3 Teleconnectivity in geopotential height fluctuations of the 500 hPa pressure surface. As in **Figure 1**, except that fluctuations are analyzed in an expanded meridional domain (0°–90° N) and period (1958–98). The correlation magnitude is contoured with a somewhat smaller interval of 0.1, and dark shading now represents values above 0.7.

the two anomaly patterns (**Figures 2A** and **4A**) are quite similar, attesting to the robustness of the PNA pattern and the analysis technique. The similarity can also be gauged by examining the pattern differences, shown in **Figure 4B**. Height differences are significant only over north-eastern Pacific and Canada, where they track the nodal lines of the PNA pattern. The pattern features over North America are, consequently, somewhat eastward shifted in the extended period analysis.

Atlantic sector teleconnection pattern The teleconnection in the Atlantic sector (**Figure 3**) represents a meridional dipole in height variability between the subtropics and higher latitudes. The teleconnection index is shown in **Figure 5D**, while its regressions on mid-tropospheric heights and zonal wind, and the sea-level pressure are shown in **Figures 5A–C**.

The 500 hPa height anomalies, shown in panel A, are confined largely to the Western hemisphere. Since the gradient of geopotential height is proportional to geostrophic wind, the variability is prominently manifest in the Atlantic jet structure, notably, though tilt changes in the jet-exit region. The mid-tropospheric height pattern is linked at the surface with an equally coherent, basin-wide fluctuation in sea-level pressure (panel B), which is largely in phase with the height pattern aloft. It is this sea-level pressure pattern, and
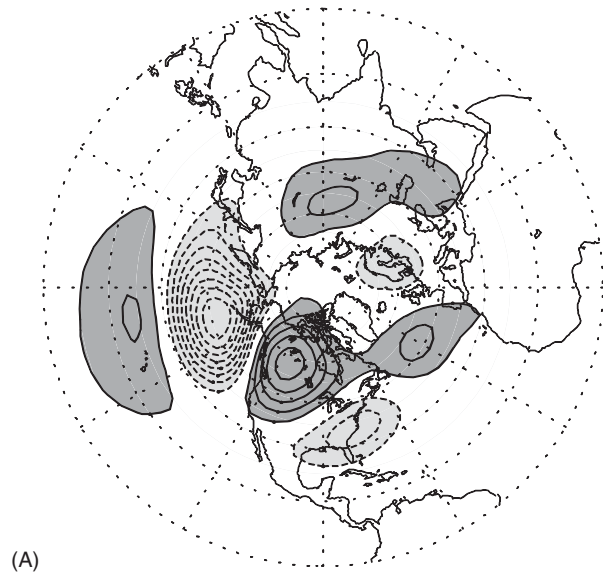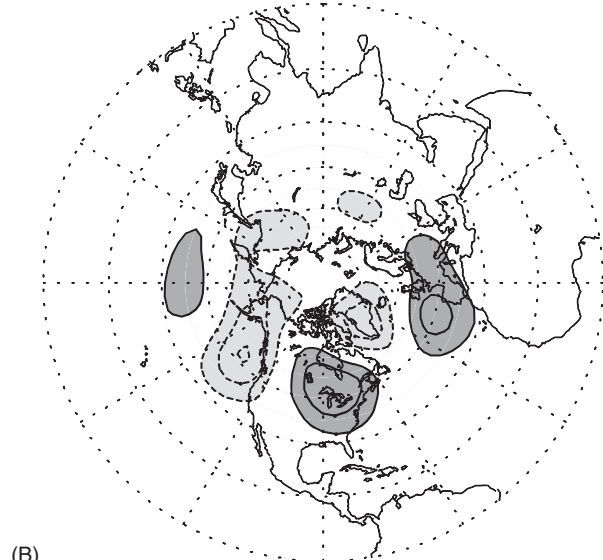
(B)

Figure 4 (A) 500 hPa height anomalies associated with the PNA teleconnection pattern during 1958–98 winters. (B) Difference in the PNA height anomalies of the two periods. The contouring interval and convention is the same as in **Figure 2A**.

its implication for the direction of near-surface winds over Europe, that is the basis for the long-standing interest in this teleconnection pattern. In the displayed phase, south-westerly flow impinges over western Europe, leading to more moderate and wetter winters in that region. In the opposite phase, near-surface winds are more zonal, and milder and wetter conditions prevail further southward over the Iberian peninsula. Not surprisingly, the amplitude and phase of this teleconnection has been monitored for well over a century, from the difference of sea-level pressure
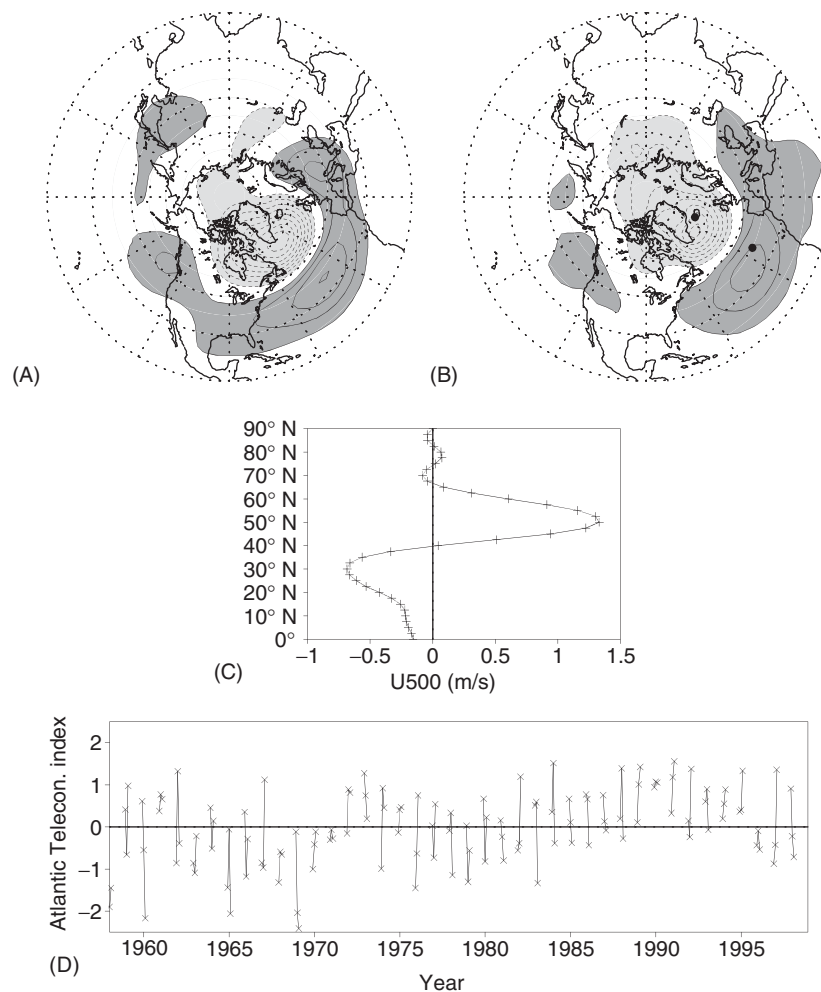
Figure 5 Variability associated with the Atlantic sector teleconnection during 1958–98 winters. A monthly index, defined using two base points in the Atlantic sector (**Figure 3**), is shown in (D). The regressed 500 hPa heights are shown in (A) with a 10 m interval, the sea-level pressure anomalies in (B) with a 1.0 hPa interval, and the zonally averaged zonal winds at 500 hPa in (C). Dark (light) shading in panels A and B denotes positive (negative) values in excess of the contouring interval, and the zero contour is suppressed. Solid dots in panel B mark Ponta Delgada, Azores and Stykkisholmur, Iceland – two stations whose sea-level pressure difference has provided a more than a century-long index for the NAO. Note that polar–stereographic projections in panels A and B begin at 15° N instead of the Equator as in earlier figures.

variations at Ponta Delgada, Azores and Stykkisholmur, Iceland; both stations are marked in **Figure 5B** using solid dots. It is noteworthy that these stations, chosen on the basis of historical surface analysis, are so well positioned with respect to the centers of the sea-level pressure pattern obtained from regression of the 500 hPa based teleconnection index.

Another view of variability associated with this teleconnection pattern is shown in **Figure 5C**, which depicts the zonally averaged zonal wind fluctuations in the mid-troposphere. This integrative, hemispheric view suggests that although variability is focused in the Atlantic sector, the polar vortex structure is also affected. The fluctuation depicted in **Figure 5C** would result in meridional contraction of the vortex, and the similarity of the mid-tropospheric and sea-level pat-

terns indicates that vortex contraction is occurring at other vertical levels as well. Expansion and contraction of the polar vortex have been reckoned to be key contributors in the generation of weather and climate variability on the basis of meteorological analysis dating back to the mid-twentieth century. These ideas are currently being reevaluated using vastly more complete sets of surface and upper-air observations, and the 'annular' viewpoint remains attractive, at least, in facilitating elucidation of the underlying processes and interactions. This is not surprising since the zonal-mean zonal flow has played a key role in advancing our understanding of the generation of the wavy component of the flow: hydrodynamic instability of the zonal-mean zonal flow provided an explanation for the occurrence of synoptic-scale wave

disturbances, while this flow's interaction with the zonally asymmetric features at the Earth's surface yielded an explanation for the presence of stationary waves in the climatological winter circulation.

An index for the Atlantic teleconnection, constructed from height anomalies at the Atlantic base points (**Figure 3**), is shown in **Figure 5D**; the monthly 500 hPa anomalies at each point are normalized before taking the difference, as for the PNA index. The Atlantic teleconnection index, like its PNA counterpart, changes phase within a winter season in almost half of the analyzed winters. On the other hand, the phase can also remain unchanged across contiguous winters: for instance, the phase is negative during 1967/68–1970/71 and positive during 1988/89–1994/95. In addition to intraseasonal variability, the Atlantic index exhibits variations on the decadal time scales, with a positive trend from 1978/79 to 1990/91.

Relationship with NAO The NAO is one of the most well-known and earliest discovered teleconnection patterns. It was identified from the analysis of sea-level pressure fluctuations in boreal winters, and generally refers to the basin-wide, meridional dipole pattern of sea-level pressure variability in the extratropical Atlantic. The extent of linkage between the surface and upper-level variability patterns is probed in this section, after characterization of NAO variability.

The NAO has recently been defined using Hurrell's monthly index, which is constructed from the difference of normalized sea-level pressure anomalies at Ponta Delgada, Azores and Stykkisholmur, Iceland. The calendar month standard deviations for the 1865–1984 period are used in normalization of the station data. The monthly NAO index is available from NCAR (http://www.cgd.ucar.edu/~jhurrell/nao.html), and is plotted in **Figure 6D** after scaling by a constant factor (0.327) so that its standard deviation in the displayed period is the same as that of the Atlantic teleconnection index (**Figure 5D**). The NAO index also exhibits variability on both intraseasonal and decadal time scales. However, unlike the Atlantic teleconnection index, an upward trend in the 1970s and 1980s is not as evident, in part due to negative excursions of the index during 1985–88. Not surprisingly, the correlation between the two monthly indices is only 0.645.

The NAO index regressions on sea-level pressure are shown in the top panel, along with the two defining stations. The station-based index is, evidently, effective in capturing the basin-wide, meridional dipole pattern of pressure variations – a pattern similar to the sea-level pressure anomalies shown earlier in **Figure 5B**. The difference between the two patterns is subtle, and best appreciated by noting the displacement of features with respect to the defining stations: the NAO pattern is meridionally tighter, and somewhat eastward displaced with respect to the other. The NAO index regressions on near-surface temperature are shown in **Figure 6B**. The 850 hPa temperature is regressed since the field is noisier at lower levels due to inhomogeneities at the Earth's surface, notably orography. The regressions reveal a coherent, large-scale pattern of warming and cooling in the middle and high latitudes. Warming occurs in regions where anomalous winds are from the south, i.e., southerly, for these winds bring warmth from the lower latitudes. Regions of strong southerly flow can be identified from the sea-level pressure pattern since winds are nearly geostrophic, i.e., almost tangential to the isobars, with lower pressures to the left in the Northern Hemisphere. An inspection of **Figure 6A** suggests that winds will have a southerly component over much of North America, and even more so over north-western Europe and Eurasia – the very regions with positive 850 hPa temperatures in **Figure 6B**. North Africa, on the other hand, is under the influence of clockwise circulation, which generates northerlies and cold advection along the eastern edge of the subtropical high-pressure cell, leading to cooling over North Africa.

The SST correlations of the NAO index (**Figure 6C**) are confined primarily to the north Atlantic, and are modest in magnitude; the maximum amplitude is only ~ 0.4, and reached near the southern tip of Greenland. A characteristic feature of the NAO SST pattern is the presence of three north-eastward oriented bands of alternating signs between the Equator and Greenland in the western/central basin. The SST warming off the European and Scandinavian coasts is comparatively modest but consequential for the downstream climate impact: in addition to the warm advection from southerly winds, marine westerlies can lead to warmer and wetter conditions over downstream landmasses, especially in the presence of warm SSTs along their west coasts. If SST warming was itself generated by surface wind anomalies – a distinct possibility – then ocean–atmosphere interaction would have served to enhance the climate impact that would have otherwise resulted. But the direction of air–sea interaction, and the role of tropical and extratropical SST anomalies in the generation of NAO variability, remains controversial. Even so, it is worth noting that while the SST pattern can be reasonably understood as arising from the influence of surface winds anomalies on heat fluxes and vertical mixing at the ocean surface, it is more difficult to understand how the Atlantic SST pattern can generate the NAO circulation anomalies.

Correlations of the NAO index with the monthly, land-station precipitation are shown in **Figure 7A**. For consistency with earlier analysis, only the 1958–98
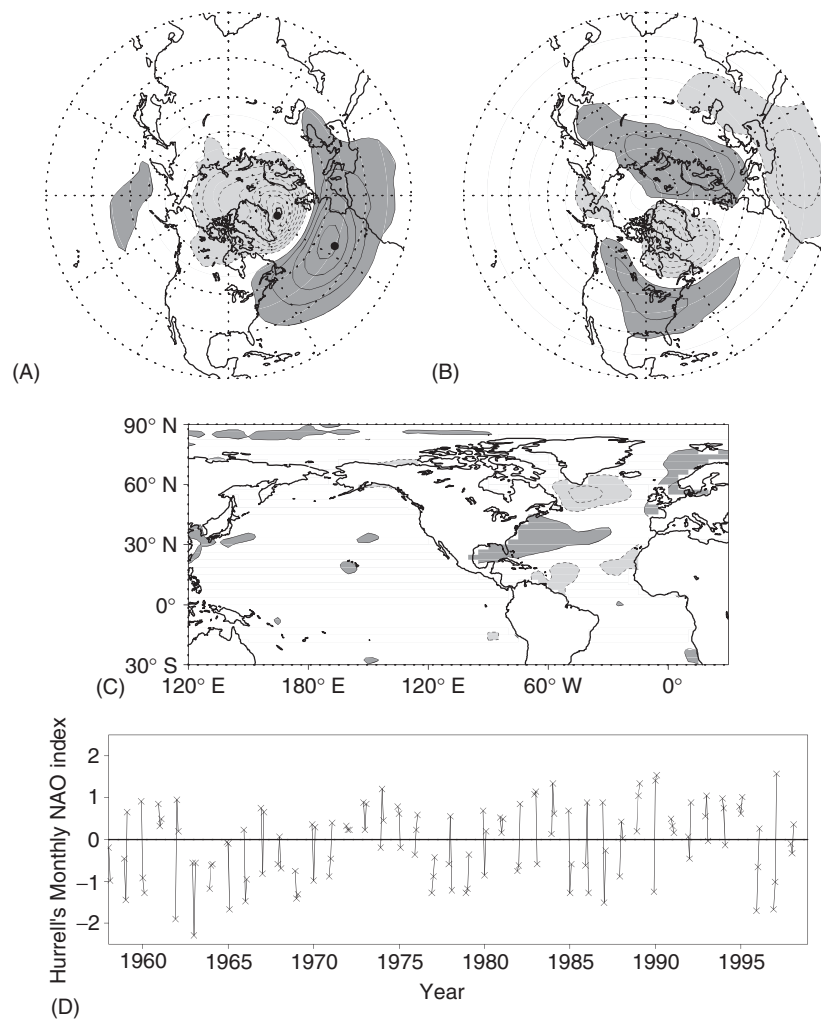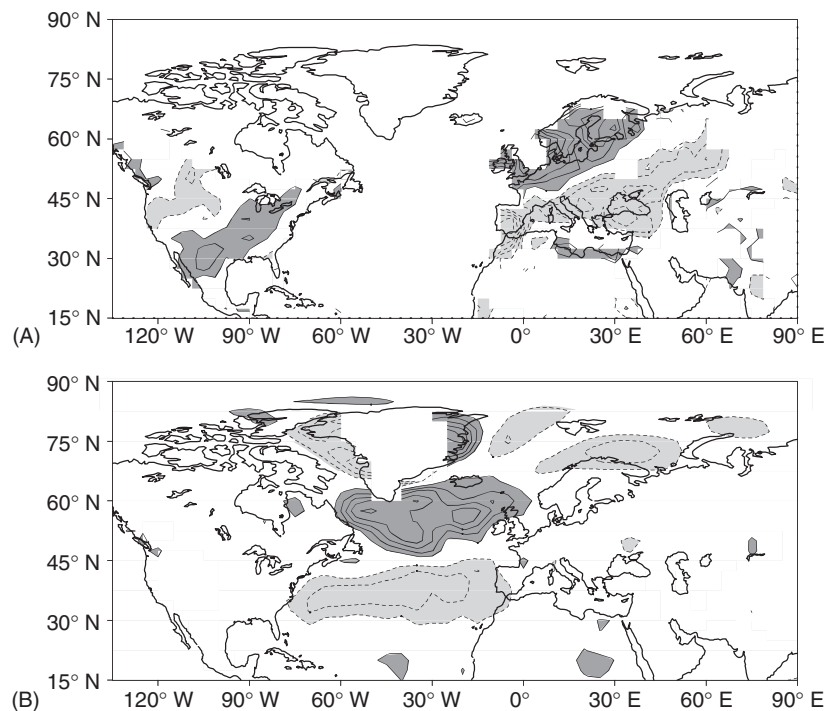
Figure 6 Variability associated with the NAO: Hurrell's monthly NAO index is shown in the bottom panel. It is scaled to have the same standard deviation as the Atlantic teleconnection index (cf. **Figure 5D**) during winter, to facilitate visual comparison. The regressed sea-level pressure and 850 hPa temperature anomalies during 1958–98 winters are contoured in panels A and B, using 1.0 hPa and 0.5° K interval, respectively. Ponta Delgada, Lisbon and Stykkisholmur, Iceland – the two stations used in the definition of the NAO index – are shown in panel A by solid dots. The sea surface temperature correlations during 1958–93 winters are shown in panel C with a 0.2 interval. The dark (light) shading in panels A–C denotes positive (negative) values in excess of the contouring interval. The zero contour is suppressed in the top three panels.

portion of the global, gridded (3.75° longitude by 2.5° latitude) data was correlated. The data set was developed by Hulme at the Climate Research Unit of the University of East Anglia, and is available from http://iridl.ldeo.columbia.edu/SOURCES/.UEA/.CRU/.Hulme/Global/. The correlation magnitude is strongest (~ 0.6) over the Iberian peninsula and north-west Europe, particularly Scandinavia. NAO's impact on western European hydroclimate can thus be characterized as a meridional dipole distribution, with warmer and wetter conditions to the north and colder and drier conditions over southern Europe and northern Africa in its positive phase. NAO's impact on North American winter precipitation, in contrast, is muted, with correlations ~ 0.2, but the correlation structure is, evidently, coherent.

Another manifestation of NAO variability is the meridional shift of stormtracks – the preferred paths of synoptic weather systems – in the midlatitudes – in the north Atlantic. Latent heating due to precipitation is the primary contributor to stormtrack heating. The heating is strongest near the surface and diminishes rapidly with height. Heating at 850 hPa is used as a marker of stormtracks here, and the anomaly associated with NAO variability is shown in **Figure 7B**. The heating is diagnosed, residually, from the thermodynamic equation and the US National Centers for Environmental Prediction (NCEP) reanalysis data for 1958–98. (Note that residual diagnosis provides an estimate of diabatic heating that is sensitively dependent on the quality of atmospheric data, particularly the divergent flow component. As such, estimates

Figure 7 Variability associated with the NAO during 1958–98 winters: (A) correlation of the gridded, monthly station precipitation over land with Hurrell's NAO index, shown with a 0.1 interval, and (B) regressed diabatic heating anomalies at 850 hPa, contoured using an interval of $0.3\,\text{K day}^{-1}$. The dark (light) shading denotes positive (negative) values in excess of the contouring interval, and the zero contour is suppressed, as before.

obtained from a different atmospheric analysis can differ to an extent.) The NAO linked heating anomalies are significant in the northern basin, being as large as $1.5\,\text{K day}^{-1}$. The basin-wide structure implies a meridional shift of stormtracks, which are climatologically centered near $40°\,\text{N}$ in the western/central basin. The stormtracks are thus poleward shifted in the positive NAO phase (displayed). Stormtrack shifts have consequences for the time-mean flow as well, since the baroclinically unstable synoptic-scale storms can transfer significant amounts of heat and vorticity in the north–south direction.

Correlation analysis provides a physically intuitive and objective method of identifying climate teleconnections, but the obtained patterns may not be independent, especially if spatial structures overlap. This, for instance, is the case in the Pacific, where three prominent patterns – PNA, the Western Pacific, and the ENSO response (shown later) – overlap to varying extent in the extratropical sector. Not surprisingly, the correlation method proved unsuccessful in capturing the ENSO response in the extratropics as a teleconnection pattern. Could this be a consequence of focusing on mid-tropospheric variability? The 500 hPa level – a level of near-zero divergence – is, perhaps, not the level of choice for identifying tropical–extratropical interactions instigated by deep convective

heating in the Tropics. Horizontal divergence associated with deep convection, such as during El Niño winters, is usually strongest in the tropical upper troposphere (~ 200 hPa). The associated midlatitude response, on the other hand, is quasi-geostrophic in character, and hence approximately non-divergent. Tropical–extratropical interactions are thus best diagnosed at a pressure level that captures the divergent outflow in the Tropics and that is near a nondivergent level in the extratropics. The 200 hPa level meets these criteria, to a large extent.

In order to ascertain the full potential of the correlation method in extracting teleconnections, the teleconnectivity map was constructed at 200 hPa from monthly height anomalies during 1958–98 winters. Except for the somewhat smaller magnitude of correlations, the 200 hPa map was very similar to the 500 hPa map displayed in **Figure 3**. In particular, the upper-tropospheric analysis did not yield any new base points, and ENSO's response in the extratropics thus remained unidentified.

Principal Component Analysis

Principal component analysis (PCA) is an elegant and widely used method for determining the structure of

recurrent variability. A common name for it is empirical orthogonal function (EOF) analysis. This method also analyzes the structure of the correlation matrix – the covariance matrix is preferred though – but focuses on regions that account for a substantial portion of the temporal variance rather than just those which exhibit strong negative correlations with distant points in the domain. In contrast with the previous method, the technique yields both the spatial patterns of recurrent variability and the extent to which these are present, or projected, in the observed anomaly record. The projection, or amplitude, is called the principal component (PC) while the spatial pattern is referred to as the loading vector (LV) in the technical literature.

Recurrent variability patterns identified from PCA are spatially and temporally independent, or orthogonal. Such a relationship among patterns is often helpful in investigating the origin and governing mechanisms of variability, but can be relaxed in one of the dimensions – space or time – if the orthogonality constraints prove restrictive. For example, it is quite conceivable for two temporally independent modes of variability to have overlapping spatial patterns. Imposition of temporal *and* spatial orthogonality constraints in this case may not lead to a physically meaningful analysis. The spatial constraint can be relaxed through the rotation of PCs, as discussed later in the section.

Consider again the variability of geopotential height, whose monthly departures from climatology are available at M latitude–longitude grid points in N winter months. As before, $\phi'_{i,k}$ represents the height departure at the ith grid point in the kth month; ϕ is an $(M \times N)$ matrix. The covariance of height departures at grid points i and j is defined as

$$\mathbf{R}_{ij} = \frac{1}{N} \sum_{k=1}^{N} \phi'_{i,k} \phi'_{j,k} = (\phi * \phi^T)/N$$

The covariance ($\mathbf{R}$) and correlation ($\mathbf{H}$) matrices are related through the scalar standard deviation field (S_i): $\mathbf{R}_{ij} = \mathbf{H}_{ij} * S_i * S_j$. Analysis of the covariance matrix is preferred since it is reasonable for regions exhibiting large variability to exert greater influence in determining the structure of recurrent variability. In the correlation matrix, the height departures are normalized by the local variance, which makes each grid point equally important. The equalization, unfairly, puts regions of large and small amplitude variability on par in the analysis. Although both metrics have been analyzed, the covariance matrix is the metric of choice in PCA. The analysis involves finding eigenvalues (λ_i) and eigenvectors ($\mathbf{E}$) of the covariance matrix ($\mathbf{R}$): $\mathbf{R} * \mathbf{E} = \mathbf{E} * \Lambda$, where Λ is a diagonal matrix of eigenvalues (λ_i), and $\mathbf{R}$, $\mathbf{E}$, and Λ are all square matrices of

dimension M. Eigenvectors of a real symmetric matrix, such as $\mathbf{R}$, are orthogonal. If they are each scaled to be of unit length as well, they become orthonormal, i.e., $\mathbf{E}^T * \mathbf{E} = \mathbf{I}$, where $\mathbf{I}$ is the identity matrix. Because of orthogonality, the projection of eigenvectors on the height anomalies, $\mathbf{C}$, can be easily obtained: $\mathbf{C} = \mathbf{E}^T * \phi$, so that $\phi = \mathbf{E} * \mathbf{C}$; $\mathbf{C}$ is an $(M \times N)$ matrix.

In meteorological analysis, the eigenvectors ($\mathbf{E}$) are commonly referred to as EOFs. The principal components ($\mathbf{P}$) and the corresponding loading vectors ($\mathbf{L}$) are closely related to $\mathbf{C}$ and $\mathbf{E}$, respectively: $\mathbf{P} = \mathbf{B}^{-1} * \mathbf{C}$ and $\mathbf{L} = \mathbf{E} * \mathbf{B}$, where $\mathbf{B}$ is a diagonal matrix of the eigenvalue square roots ($\lambda_i^{1/2}$). As in the case of EOFs, the anomaly matrix can be represented as $\phi = \mathbf{L} * \mathbf{P}$. Note that covariance of the PC and height anomalies is nothing but the corresponding loading vector: Covariance of the ith PC with anomalies at the jth spatial grid point is

$$\frac{1}{N} \sum_{k=1}^{N} P_{i,k} \Phi_{j,k} = (\phi * \mathbf{P}^T)/N$$

$$= [(\mathbf{E} * \mathbf{C}) * (\mathbf{B}^{-1} * \mathbf{C})^T]/N$$
$$= [(\mathbf{E} * \mathbf{C}) * (\mathbf{C}^T * \mathbf{B}^{-1})]/N$$
$$= [\mathbf{E} * (\mathbf{C} * \mathbf{C}^T) * \mathbf{B}^{-1}]/N$$
$$= \mathbf{E} * \Lambda * \mathbf{B}^{-1} = \mathbf{E} * \mathbf{B} = \mathbf{L}$$

Note that $\mathbf{C} * \mathbf{C}^T = N\Lambda$ was used in the above derivation; the relationship can be easily obtained from manipulation of the eigenanalysis equation.

The PCA yields a large number of spatial patterns of recurrent variability ($\mathbf{L}$), in fact as many as the number of spatial grid points; $\mathbf{L}$ is an $(M \times M)$ matrix. However, not all of them are equally significant in accounting for the temporal variance. Interestingly, the eigenvalue turns out to be a useful indicator of this significance: the spatially integrated variance is nothing but the sum of the diagonal elements of $\mathbf{R}$, i.e., the trace of $\mathbf{R}$. Since $\mathbf{R} = [(\phi * \phi^T)/N] = [\mathbf{E} * (\mathbf{C} * \mathbf{C}^T) * \mathbf{E}^T]/N = [\mathbf{E} * \Lambda * \mathbf{E}^T]$, its trace is the sum of the diagonal elements of Λ, or all the eigenvalues, λ_i. It can be easily shown that the temporal variance explained by the ith loading vector is proportional to $\lambda_i/\Sigma\lambda$. The loading vectors are thus ranked according to their eigenvalues, and only the leading ones are generally of interest.

Singular Value Decomposition

The significant PCs, LVs, and eigenvalues of $\mathbf{R}$ can be obtained from the singular value decomposition (SVD) of the anomaly matrix, ϕ. The advantage of this technique over other eigenanalysis methods is that most quantities of interest can be obtained in one step, without ever having to construct, let alone store, the covariance matrix $\mathbf{R}$, which can sometimes be very

large. The technique is, moreover, effective in extracting the significant eigenvalues and eigenvectors when $\mathbf{R}$ is not quite well conditioned.

Assuming $M > N$, the SVD of $\boldsymbol{\phi}$ results in $\boldsymbol{\phi} = \mathbf{D} * \mathbf{S} * \mathbf{V}^{\mathrm{T}}$, where $\mathbf{D}$ and $\mathbf{V}$ are square matrices of dimension M and N, respectively; $\mathbf{D}^{\mathrm{T}} * \mathbf{D} = \mathbf{I}$ and $\mathbf{V}^{\mathrm{T}} * \mathbf{V} = \mathbf{I}$, with $\mathbf{I}$ being the suitably dimensioned identity matrix. $\mathbf{S}$ is an $(M \times N)$ matrix consisting of an upper $(N \times N)$ diagonal submatrix and remaining zeroes. The N largest eigenvalues and the corresponding orthonormal eigenvectors of $\mathbf{R}$ are nothing but the first N diagonal elements of $(\mathbf{S} * \mathbf{S}^{\mathrm{T}})/N$ and column vectors of $\mathbf{D}$, respectively, i.e., $\mathbf{R} * \mathbf{D} = \mathbf{D} * [(\mathbf{S} * \mathbf{S}^{\mathrm{T}})/N]$. Note that this eigenanalysis equation is valid only for the first N column vectors of $\mathbf{D}$ (which are the same as those of $\mathbf{E}$). The projection of the N leading eigenvectors is given by $\mathbf{S} * \mathbf{V}^{\mathrm{T}}$, so the first N rows of $\mathbf{C}$ and $\mathbf{S} * \mathbf{V}^{\mathrm{T}}$ are also the same.

Rotated Principal Component Analysis

PCA provides an efficient and unique characterization of recurrent variability in terms of a small number of uncorrelated spatial patterns. The patterns are chosen so that each one successively explains the maximal residual variance in a given data set. For instance, the leading PC is obtained by requiring that it maximize the *sum* of the squared correlation between itself and the time series at all points in the analysis domain. The resulting PCs are temporally orthogonal while the LVs are spatially orthogonal. Spatial orthogonality can however be restrictive and, in many cases, undesirable, as discussed earlier. Although the leading LV is not directly impacted, subsequent LVs are often constrained to have predictable geometric relationships *vis-à-vis* the leading pattern; domain geometry, thus, becomes an influencing factor itself.

For these and other reasons, a variant of PCA analysis, called the rotated principal component analysis (RPCA), has become popular since it yields patterns that are no longer constrained to be spatially orthogonal; domain geometry is thus much less influential; rotated PCs continue to be temporally orthogonal though. The linear transformation (or solid rotation) of PCs that is widely used in meteorology is called the 'varimax' rotation. It is determined by the requirement that the *variance* of the squared correlations between each rotated PC and the original time series be maximized. Focusing on the variance, rather than sum (as in unrotated analysis), of the squared correlations increases spatial discrimination, and facilitates interpretation of the obtained patterns.

Typically, only a subset of the leading PCs are rotated. Although several criteria exist to guide the choice of this subset, the sensitivity of results to the rotated number offers good practical guidance. In most meteorological applications, 8–10 of the leading PCs are rotated; in most applications reported here, the number is 8.

Wintertime Teleconnections from RPCA

The leading patterns of recurrent height variability are extracted from RPCA and shown in **Figure 8**. The December, January, and February anomalies during 1958–98 winters were analyzed in the $30°\,\mathrm{S}$–$90°\,\mathrm{N}$ domain. Analysis was conducted at the 200 hPa level in order to also capture the tropical–extratropical interactions (e.g., ENSO-related) that are prominently manifest in the upper troposphere, for reasons stated earlier. Height anomalies were multiplied by the square root of the cosine of latitude to achieve grid-area parity, which prevents polar regions with many more points on a regular latitude–longitude grid, from unduly influencing the analysis. The covariance, rather than correlation, matrix was analyzed so that regions with large variance can exert greater control on the analysis outcome. The SVD technique was used in obtaining the PCs and LVs, and the eight leading PCs were rotated using the varimax criterion.

The leading pattern (or loading vector) is shown in **Figure 8A**. It accounts for $\sim 15\%$ of the monthly variance in the analysis domain. The height anomalies are focused in the Atlantic basin, and the pattern is very similar to the 500 hPa teleconnection in the Atlantic sector (**Figure 5A**; note the narrower display domain), except for the slight north-west shift of major features in the 200 hPa pattern. The PC associated with the upper-level pattern is shown in the top panel of **Figure 9**. Its variations in the 40 year period are similar to those of the Atlantic teleconnection index (**Figure 5D**), and even more to variations of the Hurrell index (**Figure 6D**). The PC's correlation with the Hurrell index is, in fact, 0.84, which is significantly larger than the correlation of the Atlantic teleconnection and Hurrell indices (0.645). RPCA has thus yielded a pattern that is more closely linked with Hurrell's NAO index.

The second leading pattern, shown in **Figure 8B**, represents higher geopotential heights in all sectors of the northern subtropics, but especially over the central/eastern Pacific. Higher upper-level heights are typically associated with a warmer air column underneath, since the atmosphere is in hydrostatic balance. The pattern of variability is thus associated with a warming of the Tropics, such as that seen during ENSO winters. The presence of a subtropical ridge to the south-east of the Hawaiian Islands is also indiqcative of linkage with ENSO, for deep convection in this tropical Pacific sector during ENSO winters and
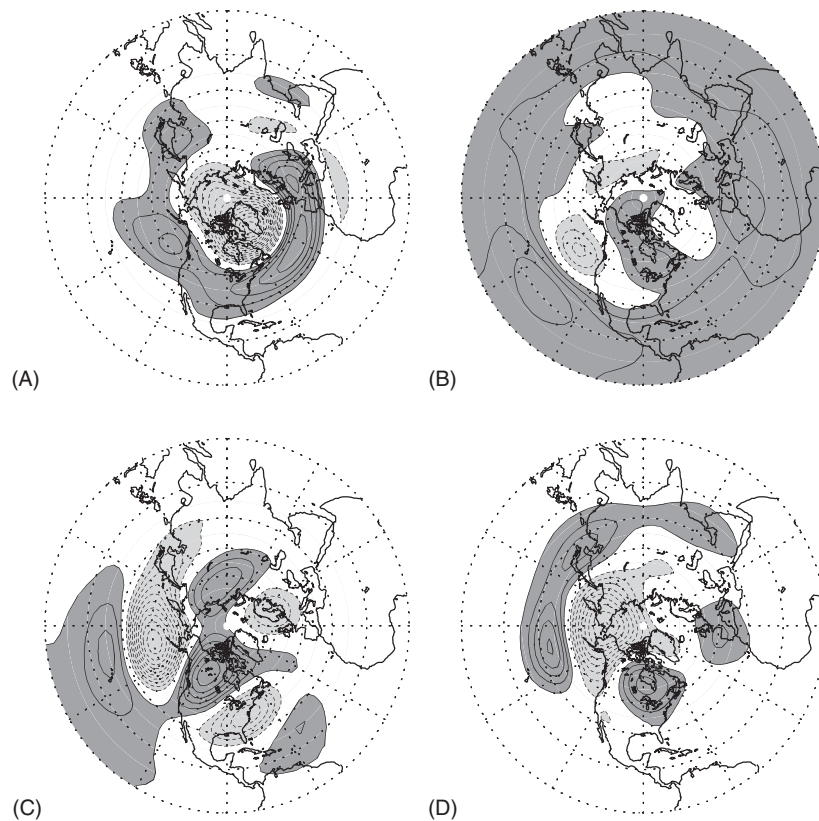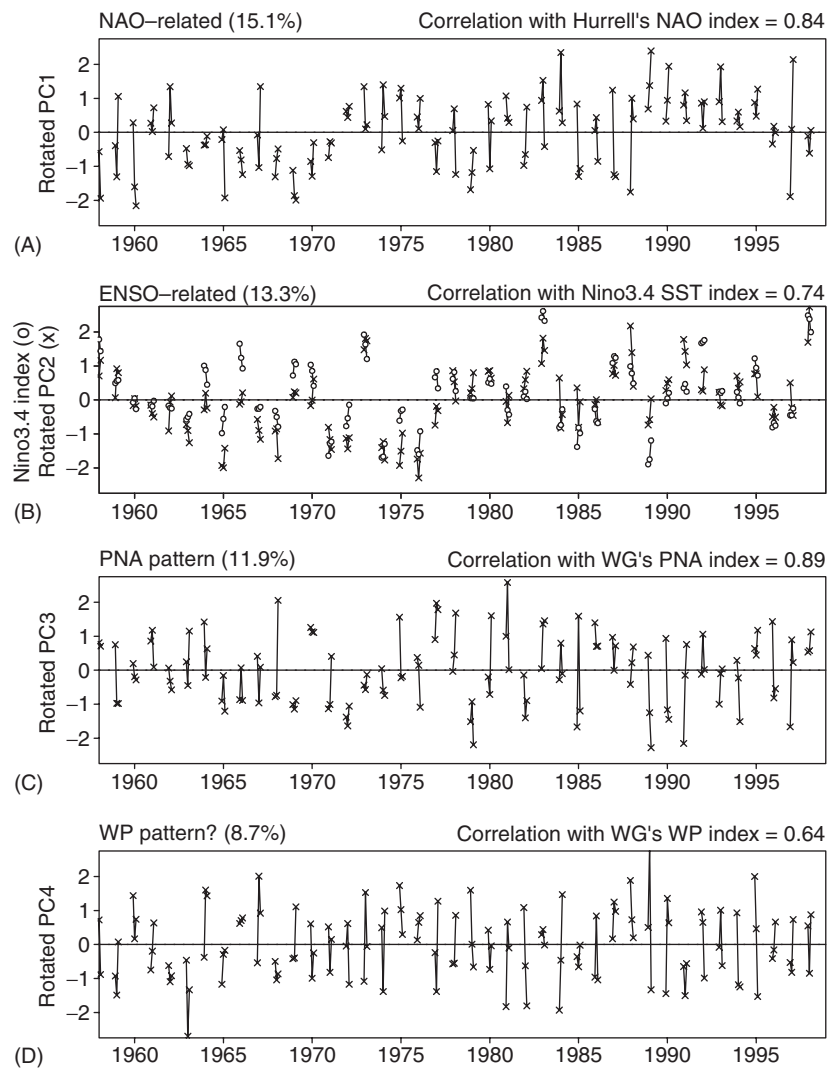
Figure 8 Leading patterns of height variability at 200 hPa, obtained from rotated PCA: (A) NAO-related, (B) ENSO-related, (C) PNA pattern, and (D) the WP pattern. The covariance of monthly fluctuations in the 30° S–90° N domain is analyzed in Northern winter (December, January, and February) during January 1958–February 1998. Eight leading PCs are rotated using the varimax criterion (see text for more details). Height anomalies in panels A–D are contoured with an interval of 10 m, and dark (light) shading denotes positive (negative) values in excess of the contouring interval. The zero contour is suppressed. Patterns A–D explain 15.1%, 13.3%, 11.9%, and 8.7% of the domain-averaged variance.

the related divergent outflow are linked with the development of an upper-level anticyclonic circulation in the subtropics. The anomaly structure resembles the characteristic height response during ENSO winters, which is shown in **Figure 10A**; the annular structure in the Tropics is again noteworthy. The characteristic response is obtained from regressions of the Niño3.4 SST index, which is a widely used marker of ENSO variability. Although the amplitude of features over North America is weaker in **Figure 8B**, their position is reasonable. In both figures, the ridge is located between the Great Lakes and Hudson Bay, and not over the Pacific/Northwest (the case in the PNA pattern). The position of the subtropical ridge off the Hawaiian Islands (and even the weaker one over south-western Europe) is quite similar in both maps.

The PC associated with this LV is shown in **Figure 9B**, and accounts for ∼13% of the monthly variance during winter. Also shown in this panel is the Niño3.4 SST index, which is the average SST in an equatorial Pacific box (5° S–5° N, 170–120° W; marked in **Figure 10C**). The index is normalized, just

as the PC, and shown using open circles ('o'). The correlation between the PC and the index is 0.74. Inspection of the two time series shows that correlations are not higher, primarily because the PC was unable to capture aspects of ENSO variability prior to the 1976/77 climate transition: El Niño events during the 1960s were, in particular, missed. The second leading PC is thus related to ENSO variability, even though it falls short of providing a full representation of its spatial and temporal structure. It is remarkable that RPCA of upper-tropospheric heights can identify ENSO-related variability without any reference to the underlying SST variability. Note that teleconnection analysis of the 200 hPa height variability in the same period was unsuccessful in this regard.

The third leading pattern of winter height variability, shown in **Figure 8C**, is clearly the PNA pattern. It explains ∼12% of the domain-averaged variance, and stands out because of its coherent, arcing structure. Except for minor embellishments of the tropical features, the displayed structure is quite similar to that shown in previous depictions (**Figures 2A** and **4A**),

Figure 9 Leading PCs of height variability at 200 hPa, obtained from rotated analysis: (A) NAO-related, (B) ENSO-related, (C) PNA, and (D) the WP PCs. The amount of variance explained by each PC is indicated in % in the title line. For comparison, the normalized Niño3.4 SST index is displayed in panel B using the 'o' symbol. PC correlations with popular indices of related phenomena are also shown in the title line.

which were all at the 500 hPa level. It is interesting to compare the position of the subtropical ridge in the PNA and ENSO-related patterns, since this can be helpful in identification: the ridge is centered westward of the Hawaiian Island in the former, but southeastward of the islands in the latter pattern. The associated PC is shown in **Figure 9C**. Its correlation with the PNA index (α_{PNA}; defined earlier in text using the 500 hPa height anomalies) is 0.89.

The fourth leading variability pattern identified by RPCA is shown in **Figure 8D**. It is referred to as the Western Pacific (WP) pattern, since its structure is broadly similar to the teleconnection pattern bearing the same name. Although the pattern is focused in the Pacific basin, its structure bears close resemblance to

the Atlantic sector pattern (**Figure 8A**): meridionally dipolar structure with a node near 45°N; larger amplitude of the polar cell; height anomalies focused in the jet longitudes (Asian-Pacific and Atlantic), especially the jet-exit sectors; a more zonally extended, weaker southern cell, with 4–5 local maxima. Interestingly, the maxima in the Eastern Hemisphere of both patterns are in the same longitudinal sectors, reflecting perhaps the wave-guiding influence of the climatologically prominent Asian-Pacific jet. The WP pattern exhibits direct regional resemblance to the PNA and ENSO-related patterns too: Despite subtle shifts, there is some correspondence with the PNA features over the extratropical Pacific, and with the ENSO-related pattern features over North America.

The latter correspondence, in fact, contributed to erroneous linkage between the WP pattern and ENSO variability in early investigations of climate teleconnections. The PC associated with the WP pattern is shown in **Figure 9D**. Unlike the ENSO-related PC (or Niño3.4 index), the WP pattern's PC exhibits substantial intraseasonal variability, with phase changing within a season in two–thirds of the analyzed winters. Not surprisingly, its correlation with the Niño3.4 index is only 0.10. For reference, the PC correlation with the WP teleconnection index, defined using the two western Pacific base points in the teleconnectivity map shown in **Figure 1**, is 0.64.

RPCA of ϕ_{200} and SST Variability

The analysis of combined variability of the upper-level geopotential and SST anomalies is motivated by the need to clearly identify the ENSO-related height pattern in Northern winter months. Further clarification of ENSO's characteristic height response should be beneficial for the other modes as well, in view of aliasing of the misrepresented structure. Differences between height regressions of the Niño3.4 SST index and the ENSO-related pattern obtained from RPCA of ϕ_{200} (**Figures 10A** and **8B**, respectively) indicate potential shortcomings of the analysis strategy, arising, perhaps, from the lack of consideration of the underlying SST structure in determination of the recurrent variability patterns. Alternatively, the differences could be construed as questioning the suitability of the Niño3.4 SST index as a marker of ENSO variability: a non-issue, since other modes of Pacific SST variability, including the decadal ones, have little signal in the Niño3.4 region.

Modes of recurrent ϕ_{200} and SST variability are extracted by simultaneously analyzing the structure of
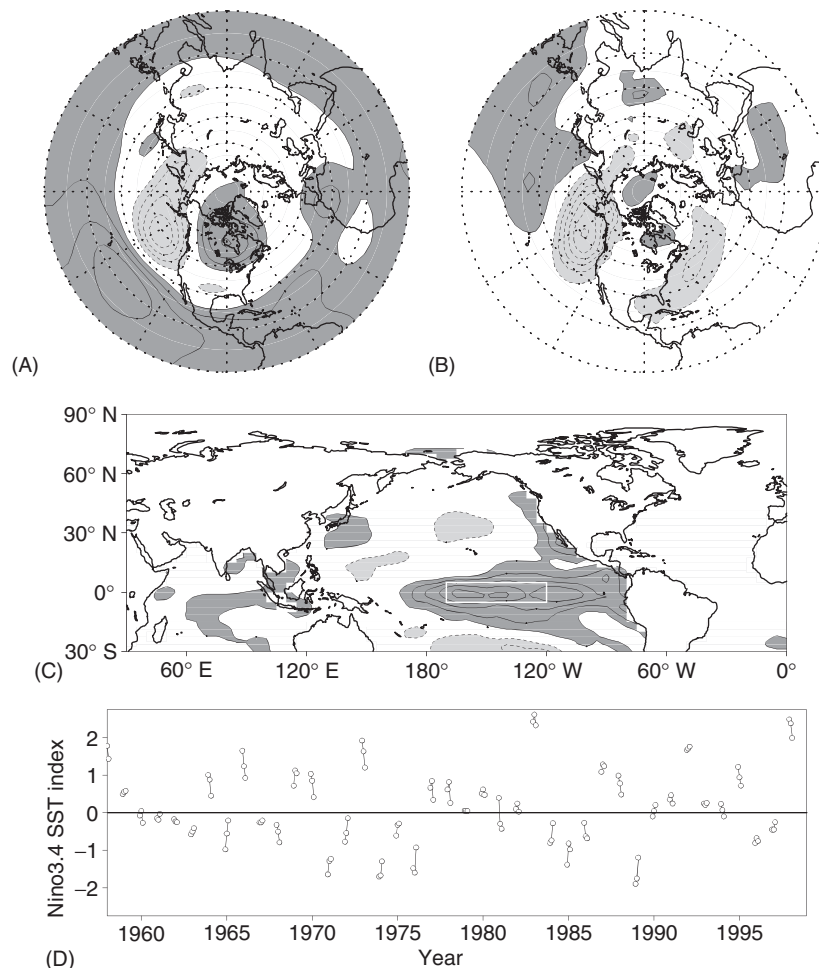
Figure 10 ENSO variability. The Niño3.4 index, which is the average SST anomaly in the marked equatorial Pacific box, is shown in the bottom panel. The index is scaled to have the same standard deviation as the PCs shown in **Figure 9**. The regressed 200 hPa geopotential height and sea-level pressure anomalies during 1958–98 winters are contoured in panels A and B using 10 m and 0.5 hPa intervals, respectively. The SST regressions during 1958–93 winters are shown in panel C with a 0.2 K intervals. The dark (light) shading in panels A–C denotes positive (negative) values in excess of the contouring interval. The zero contour is suppressed in the panels.

the auto-covariance and cross-covariance matrices in the 30° S–90° N domain. As before, each variable was multiplied by $(\cos \theta)^{1/2}$ to achieve grid-area parity on a regular longitude–latitude grid. The individual variables were, moreover, put on par by dividing their anomalies by the square root of the sum of temporal variance over that variable's spatial grid. The normalization allows regions with larger variance to have more influence on the analysis outcome, but at the same time maintains parity between the overall influence of each variable. In view of the shorter ship-based SST record, the combined analysis was conducted for the 1958–93 subperiod. To offset the shorter record, monthly anomalies in an expanded winter season (December–March) were analyzed. The SVD technique was used in obtaining the PCs and LVs, and the eight-leading PCs were rotated using the varimax criterion, all as before.

The leading mode of combined variability is shown in **Figure 11**. It explains ∼14% of the monthly geopotential and SST variance in winter in the analysis domain. Note that the explained variance is small since the total variance that needs to be accounted for is now that of two variables; the analysis domain is moreover very large, larger than the Northern Hemisphere. (In more regional domains, the explained variance amounts would be much bigger.) The close similarity of the modal structure with Niño3.4 regressions (**Figure 10**) indicates that this mode represents ENSO variability with considerable fidelity. Major features of the upper-level height pattern, including the ones over North Pacific and North America, are now stronger and more closely aligned with the target pattern (**Figure 10A**) than those depicted in **Figure 8B**. The SST component of the leading mode (**Figure 11C**) shows a pronounced,
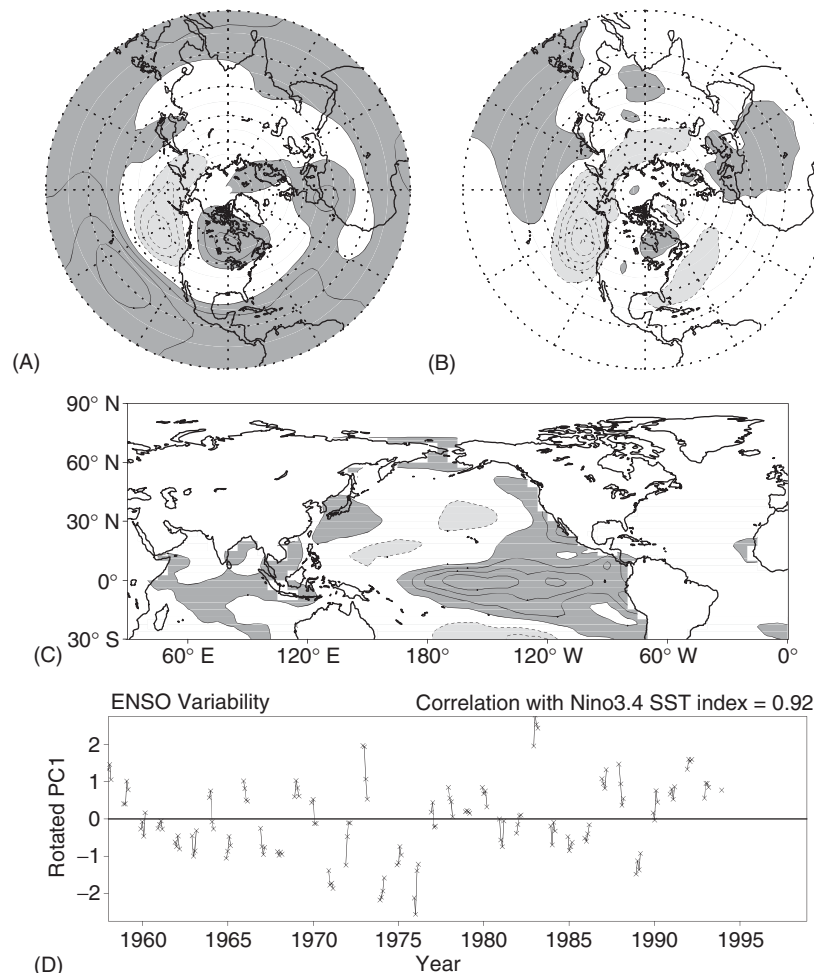
Figure 11 ENSO variability: RPCA of combined variability of the 200 hPa geopotential height and SST anomalies during 1958–93 winter months (December–March). The leading mode explains ∼14% of the height and SST variance in the 30° S–90° N domain. The 200 hPa height and regressed sea-level pressure anomalies are contoured in panels A and B using 10 m and 0.5 hPa intervals, respectively. The SST component of the leading mode is shown in panel C with a 0.2 K interval. The dark (light) shading in panels A–C denotes positive (negative) values in excess of the contouring interval. The zero contour is suppressed in the panels.

zonally extended anomaly in the central and eastern tropical Pacific, with amplitude in the Niño3.4 region approaching 1.0 K. The SST anomaly pattern is strikingly similar to SST regressions of the Niño3.4 index during Northern winter (**Figure 10C**). The similarity is not confined to the tropical Pacific, but extends well into the subtropics and other ocean basins, particularly the Indian Ocean. Not surprisingly, the correlation between the leading PC (**Figure 11D**) and the Niño3.4 SST index is 0.92. The leading mode of combined variability thus represents the mature phase of ENSO variability, since ENSO-related SST and circulation anomalies attain their largest amplitude generally during Northern winter and early spring months.

The ENSO-related sea-level pressure anomalies are contoured in **Figure 11B** (or **Figure 10B**) using a 0.5 hPa interval. The interval is half of that used before in displaying the sea-level pressure anomalies in the extratropics. A smaller contour interval is used here in order to capture the sea-level pressure variations in the Tropics, which are generally weaker than their mid-latitude counterparts because of the smaller Coriolis parameter ($= 2\Omega \sin \theta$, where Ω is the Earth's rotation rate and θ the latitude). Smaller Coriolis force allows for stronger divergent circulations in the Tropics which, in turn, weaken pressure gradients. The reduced interval detects the higher sea-level pressure in the western tropical Pacific but, evidently, not in the central and eastern portions of the basin where pressure is lower during ENSO episodes, but by an amount smaller than the contour interval. In the extratropics, sea-level pressure is lower along the US west coast and the Gulf Coast, and over Florida, which leads to enhanced precipitation in these regions during El Niño winters.

The second leading mode of combined variability is shown in **Figure 12**, and represents NAO variability. The mode accounts for ∼10% of the monthly geopotential and SST variance. The 200 hPa height anomalies are focused in the Atlantic basin, and the pattern is very similar to that obtained from RPCA of heights alone (cf. **Figure 8A**). The SST component (panel B), on the other hand, is very similar to the SST correlations of Hurrell's NAO index (**Figure 6C**), except for the stronger amplitude: particularly in the northern tropical Atlantic, where correlations approach 0.5. It is noteworthy that NAO variability is not correlated with tropical Pacific SSTs, at least contemporaneously during Northern winter months. The PC is shown in the bottom panel, and its correlation with Hurrell's monthly NAO index during 1958–93 winters is 0.77.

The third leading mode obtained from the analysis of upper-level heights and SST variability is shown in

Figure 13. It accounts for ∼6% of the combined variance, and represents PNA variability. The 200 hPa height pattern (panel A) is very similar to that obtained earlier from RPCA analysis of height variability alone (**Figure 8C**), except for the meridionally tighter structure of the subtropical ridge located upstream of Hawaii. The SST component (panel C) is broadly similar to SST correlations of the PNA index during 1962/63–1976/77 winters (**Figure 2C**), in that correlations are strongest in the extratropical Pacific. Analysis of combined variability reinforces the linkage with Pacific midlatitude SSTs, by showing PNA variability to be even more uncorrelated with SST in the tropical Pacific and other ocean basins, at least contemporaneously. The PNA PC is displayed in the bottom panel, and is correlated with the PNA index at 0.84, and with Niño3.4 SST index at 0.07. The PC regressions on sea-level pressure are displayed in **Figure 13B**, and should be compared with the corresponding regressions of the PNA index shown earlier in **Figure 2B**. The comparison indicates that analysis of combined variability leads to a PNA structure that is tightly focused in the extratropical Pacific basin.

Recalling that identification of ENSO's characteristic height response in the mid-troposphere is difficult regardless of the analysis method – in part, because tropical features that facilitate pattern discrimination at other levels are very weak in the mid-troposphere – it is of some interest to examine the structure of PNA and ENSO height responses in this region. The mid-tropospheric structures are obtained by regressions of the ENSO and PNA PCs on 500 hPa height anomalies, and shown in **Figure 14**. The PCs themselves are from the earlier analysis of combined variability of 200 hPa heights and SST (**Figures 11D** and **13D**). The PNA anomalies in **Figure 14** are shaded while the comparatively weaker ENSO ones are shown using thick lines. The analysis of combined variability has yielded a clear separation of the two variability patterns in the mid-troposphere – a challenging task given the much weaker amplitude of the ENSO pattern. In the midlatitudes, the patterns are nearly in quadrature, with nodal lines of one intersecting the extremum zones of the other over North Pacific and North America. It is worth noting that the analysis method has not imposed a spatial orthogonality constraint on the patterns, since the latter are obtained from a rotated analysis.

The temporal structure of ENSO and PNA variability is examined in **Figure 15**. The two PCs are constrained to be temporally orthogonal by the analysis method. The examination is thus motivated by questions related to linkage of the two modes when their amplitude is large: for example, is significant amplitude PNA variability excited more frequently
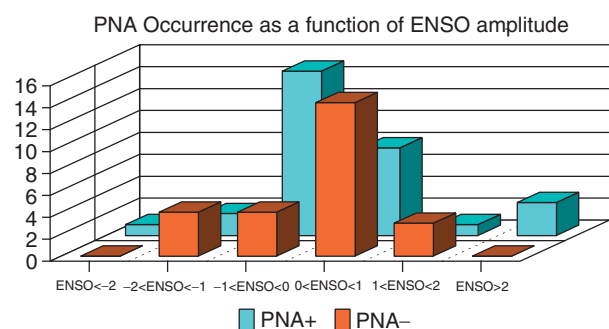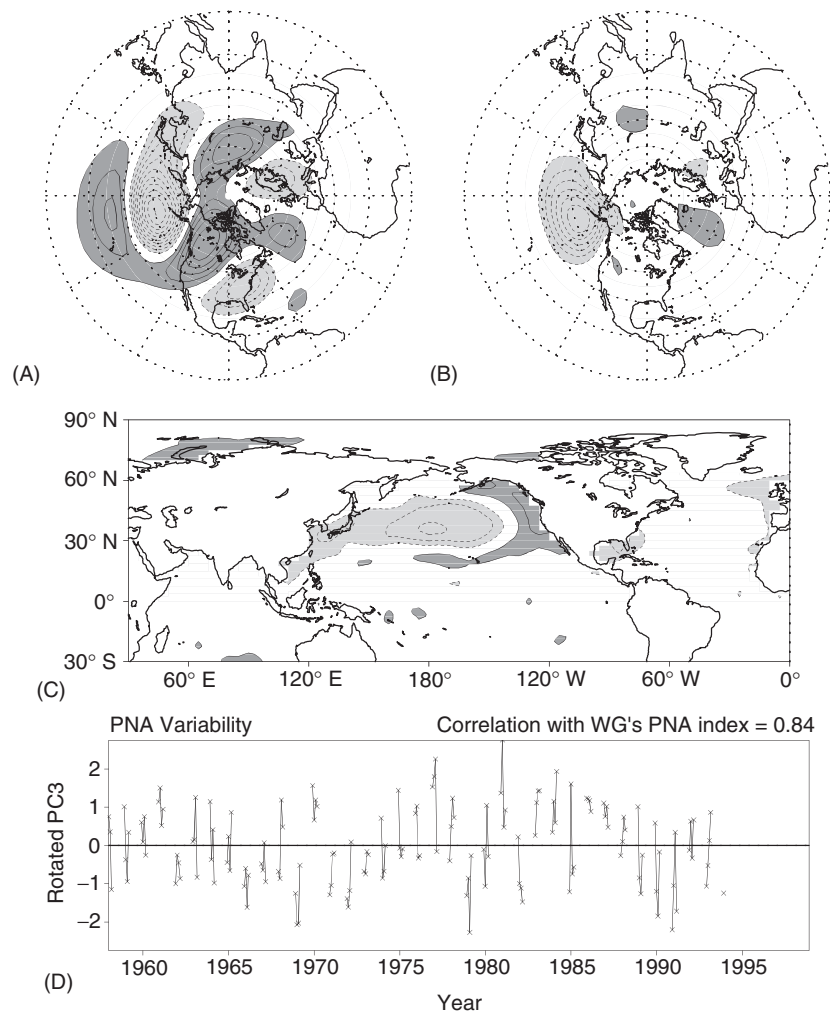
(A)

(B)

(C)
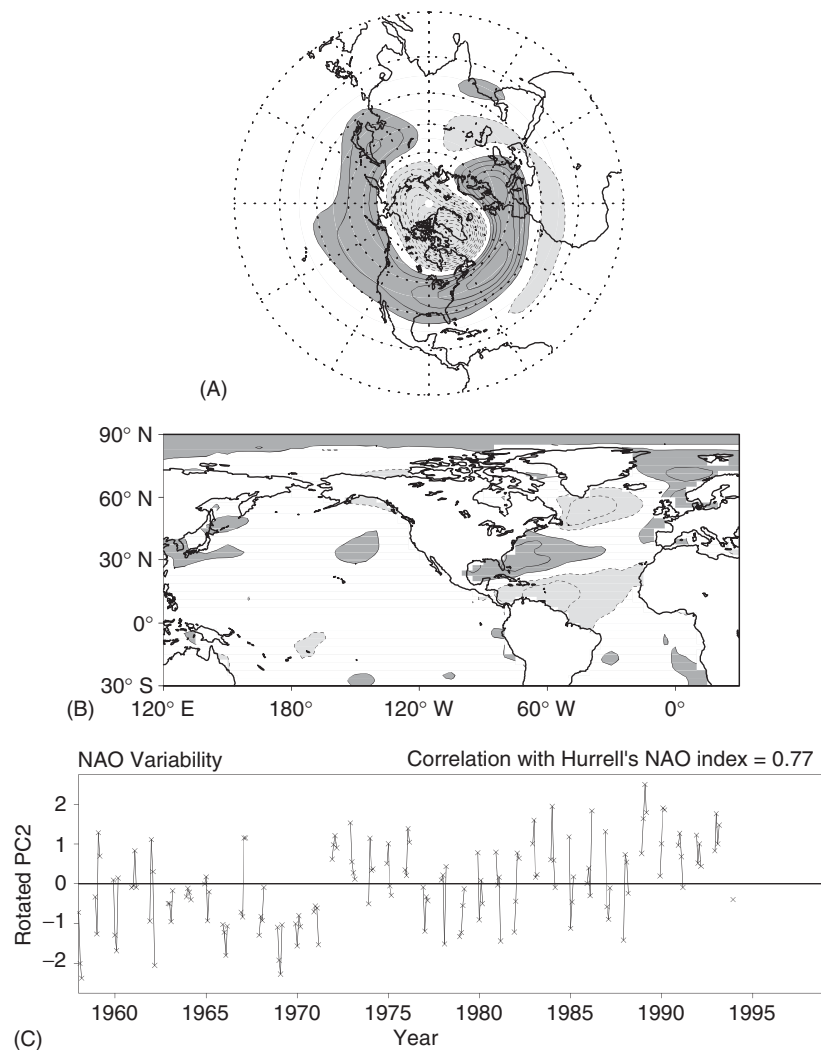
Figure 12 NAO: from RPCA of combined variability of the 200 hPa geopotential height and SST anomalies during 1958–93 winter months (December–March). The 2nd leading mode explains ∼10% of the height and SST variance in the 30° S–90° N domain. The 200 hPa height is contoured in panel A using a 10 m interval while the SST component is shown in panel B using *correlation* contours, with a 0.2 interval. The dark (light) shading in panels A and B denotes positive (negative) values in excess of the contouring interval. The zero contour is suppressed in all panels.

(and in a given phase) during El Niño episodes? A scatter plot of the two PCs facilitates investigation of such questions. The linkage question is, of course, meaningful only in the context of PNA occurrences of significant amplitude. In subsequent analysis, the patterns are considered to have significant amplitude when their PC magnitude exceeds 1.0.

The distribution of significant amplitude PNA events with respect to ENSO variability is examined first, by binning such events in ENSO PC intervals of 1.0, as shown in the bar graph. The number of positive-phase PNA occurrences is shown in blue while the corresponding negative-phase number is displayed in red. For most ENSO amplitudes, the difference between the positive- and negative-phase PNA occurrences is quite small, and not statistically

meaningful. The same difference is however large and potentially significant in weak ENSO conditions. For example, weak La Niña events ($-1.0 <$ ENSO PC < 0) appear to be conducive for the generation of

Figure 13 PNA variability: from RPCA of combined variability of the 200 hPa geopotential height and SST anomalies during 1958–93 winter months (December–March). The 3rd leading mode explains about 6% of the height and SST variance in the 30° S–90° N domain. The 200 hPa height and regressed sea-level pressure anomalies are contoured in panels A and B using 10 m and 1.0 hPa intervals, respectively. The SST component is shown in panel C using correlation contours, with a 0.2 interval. The dark (light) shading in panels A–C denotes positive (negative) values in excess of the contouring interval. The zero contour is suppressed in the panels.

significant amplitude +ve PNA variability. Inspection of **Figure 15** shows that not only are there more +ve PNA events, but that some of the largest amplitude ones occur during weak La Niña conditions. The opposite appears to be the case during weak El Niño conditions, which evidently favor the negative phase of PNA variability; the phase bias is however not as pronounced as in weak La Nina conditions. The − ve PNA phase is however not preferred during strong El Niño conditions, an event category exhibiting some preference for the +ve PNA phase; sampling concerns, however, preclude drawing conclusions, here. It is worth noting that the phase bias manifest in the above bar graph is not a consequence of the temporal orthogonality constraint imposed in PCA, as such a condition may only require the amplitude of one pattern to be large when the other's is small.
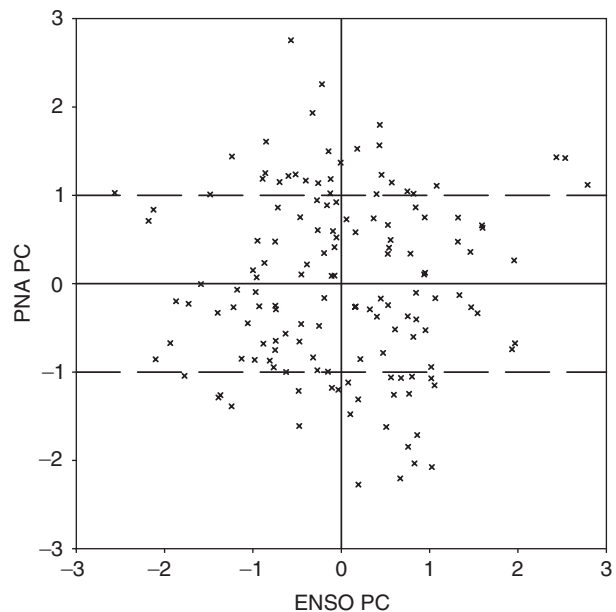
WP variability pattern/North Pacific Oscillation The fourth leading mode of combined variability is referred to as the WP pattern. It explains about 5% of the geopotential and SST variance, and is shown in **Figure 16**. The small fraction of the accounted variance does not indicate insignificance of this mode, but is rather a reflection of the consideration of two variables in a large spatial domain, as noted earlier. The WP pattern represents both intraseasonal and lower-frequency variability over the North Pacific. The meridionally dipolar height pattern is associated with latitudinal displacements of the Asian-Pacific jet, and linked at the surface to a long known pattern of sea-level pressure variability, the NPO. The upper-level trough is centered over the Bering Strait but extends south-eastward along the west coast of North America, while the ridge to the south extends
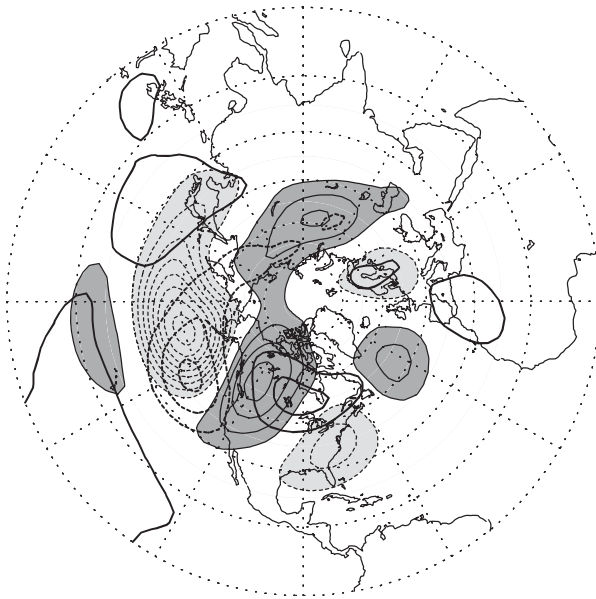
Figure 14 The 500 hPa height regressions of the ENSO and PNA PCs. The PCs were obtained from the combined analysis of 200 hPa geopotential height and SST anomalies, and shown in the previous two figures. The PNA regressions are shaded while the ENSO ones are contoured using thick lines. The contour interval is 10 m, and dark (light) shading denotes positive (negative) values in excess of the contouring interval. The zero contour is suppressed, as before.

Figure 15 Scatter plot of the ENSO and PNA PCs during the 1958–93 winter months (December–March). The PCs were obtained from the combined analysis of 200 hPa geopotential height and SST anomalies, and shown earlier in **Figures 11** and **13**. The long-dash lines help to focus on the stronger PNA occurrences, which lie above (below) the PNA PC = +1 (− 1) lines.

from the Korean peninsula to the Hawaiian Island longitudes. Height anomalies are however not confined to the Pacific sector alone: a split ridge is present over the north Atlantic, with one lobe over southern Hudson Bay and the other positioned in the vicinity of the British Isles. Sea-level pressure regressions are displayed in panel B, and show a zonally elongated high-pressure cell spanning the Pacific longitudes. The surface-low to the north is centered eastward of the upper-level trough, implying a westward tilt with height of the higher-latitude anomalies. In contrast, the high-pressure cell over the British Isles is located just underneath the upper-level ridge, i.e., in an equivalent barotropic configuration. The surface-low extends sufficiently south-eastward to be of some consequence for hydroclimate variability over North America, including the US Great Plains.

The SST component of the variability mode is shown in panel C, using the correlation measure. Correlations approach 0.4 in both the midlatitude and tropical sectors of the Pacific; a smaller contour interval, 0.15, is used in this panel. Significant correlations with tropical Atlantic SSTs are also evident. The correlations in the Pacific basin – the boomerang structure in particular – are reminiscent of the structure of Pacific decadal SST variability. The 36 year record analyzed here is too short, though, to charac-

terize decadal time-scale variability, but the structural correspondence is nonetheless intriguing. The PC, displayed in panel D, depicts both the intraseasonal and lower-frequency nature of WP variability. The pattern's phase changes within a season during most of the analyzed winters, but a lower-frequency modulation of amplitude is also evident. For example, the termination of an upward trend, or Pacific cooling, after the 1975/76 winter, which has been noted in other analyses, is reflected in the PC distribution. The PC correlation with Wallace and Gutzler's WP teleconnection index is 0.45. There are several reasons for this small correlation, not the least of which is the much shorter period of that teleconnection analysis: The WP structure, particularly the component linked with low-frequency interannual variability, would be difficult to characterize from analysis of a 15-winter long record. Correlations are also small because of potential aliasing of ENSO variability in the earlier analysis.

Impact on Northern Hemisphere precipitation The monthly land-station precipitation correlations of the four variability modes are shown in **Figure 17**. As before, the correlations are for the 1958–93 winters (December–March), and obtained using principal components from the rotated analysis of ϕ_{200} and
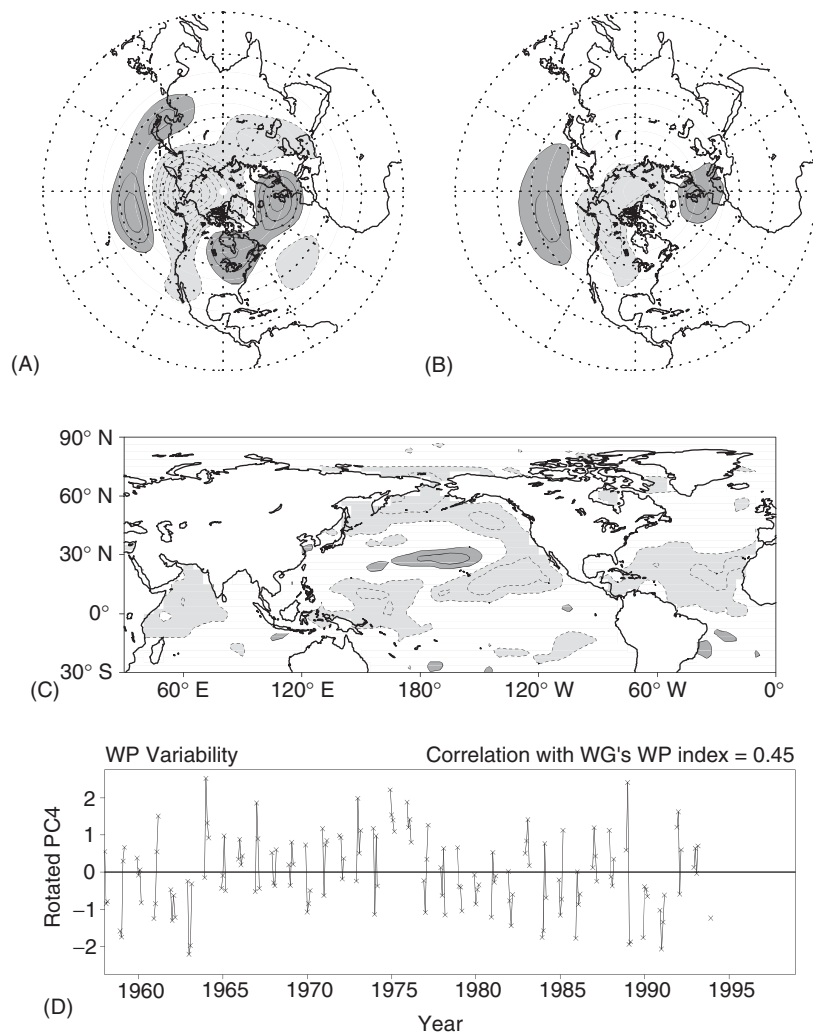
Figure 16 WP variability: from RPCA of combined variability of the 200 hPa geopotential height and SST anomalies during 1958–93 winter months (December–March). The 4th leading mode explains about 5% of the height and SST variance in the 30° S–90° N domain. The 200 hPa height and regressed sea-level pressure anomalies are contoured in panels A and B using 10 m and 1.0 hPa intervals, respectively. The sea surface temperature *correlations* are shown in panel C with a 0.15 interval. The dark (light) shading in panels A–C denotes positive (negative) values in excess of the contouring interval. The zero contour is suppressed in the panels.

SST variability. The ENSO correlations in the El Niño phase are shown in panel A, and broadly indicate a southward shift of precipitation over North America. The correlations are large (0.3–0.4) over the US west coast, southwestern states, and Flordia, and over Mexico. The NAO correlations are shown in panel B, and are similar to those shown and discussed earlier (cf. **Figure 7A**). Noteworthy features include the meridional dipole distribution over Europe, with wetter conditions to the north, and the comparatively muted signal over North America. The PNA correlations, in contrast, are strong over the Pacific Northwest and the eastern US region centered on the Ohio river valley. The WP/NPO correlations are of some significance in the Pacific Northwest and in the northern Great Plains. Note that the correlations would generally be larger had the seasonal-mean anomalies been analyzed.

Similarity between WP/NPO and NAO variability The similarity of the two variability modes is investigated next, prompted in part by the resemblance of their surface signatures. The pioneering analysis of sea-level pressure fluctuations by Walker and Bliss characterized the winter structure of the Pacific and Atlantic basin anomalies – the North Pacific and North Atlantic oscillations – and pointed out the correspondence in features. The characterization of NAO structure is on firmer footing though, since the Atlantic is 'data rich' in comparison with the Pacific.

The sea-level pressure regressions of the two PCs (**Figures 12C** and **16D**) are shown in **Figure 18**, with
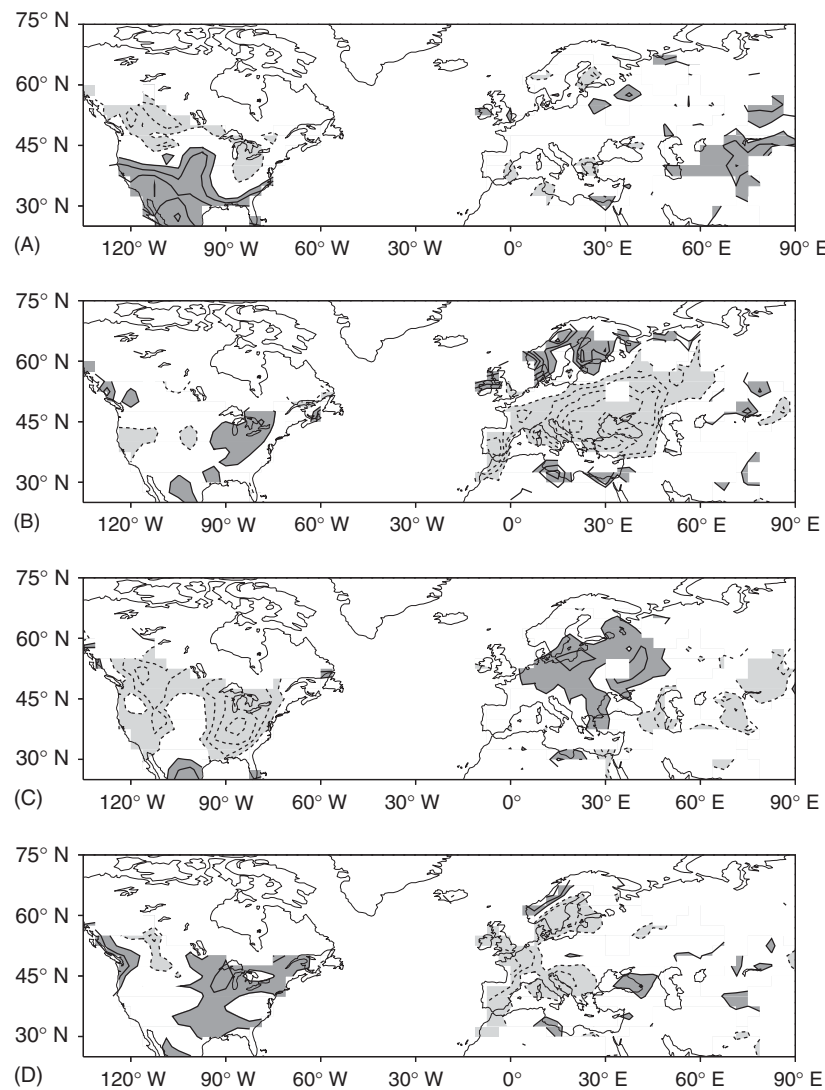
Figure 17 Correlation of the gridded, monthly station precipitation over land with the four leading PCs obtained from rotated analysis of 200 hPa height and SST variability: (A) ENSO, (B) NAO, (C) PNA, and (D) WP/NPO. Correlations are shown for the December–March period, and for the previously displayed phases of these variability patterns. The contour interval is 0.1. The dark (light) shading denotes positive (negative) values in excess of the contouring interval, and the zero contour is suppressed, as before.

the maps rotated so that both ocean basins are in the 6 o'clock position, to facilitate comparison. The zonally elongated, seesaw structure, with a node at $\sim 50^{\circ}$ N, and a third center at ~ 12 o'clock position, is evident in both patterns. The patterns are moreover located in the jet-exit region of the climatological jets in each basin, the Asian-Pacific and the Atlantic jets. A comparison with the corresponding upper-level height patterns indicates a vertically coherent structure of the midlatitude anomalies in the two basins. Given the proximity to the climatological jets, it is of some interest to examine the impact of WP/NPO and NAO variability on the tropospheric jet structure. Panels C and D depict the latitude-height structure of the climatological (thick solid contours) and anomalous

(thin shaded contours) zonal wind in each basin. The longitudinal average is restricted to the 150° E–135° W sector in the Pacific basin and to the 80° W–0° sector in the Atlantic. The sectors are chosen on the basis of the zonal extent of the sea-level pressure anomalies, and sector boundaries are marked in panels A and B using thick meridian lines.

Superposition of the sector-averaged zonal wind anomalies on local jet structure shows that the WP/NPO variability pattern latitudinally shifts the Asian-Pacific jet. In the depicted phase (**Figures 16**), the tropospheric jet is shifted poleward, and the polar vortex is strengthened in the Pacific lower strato-sphere. A rather similar distribution of anomalies is evident in the Atlantic sector. Although the climato-
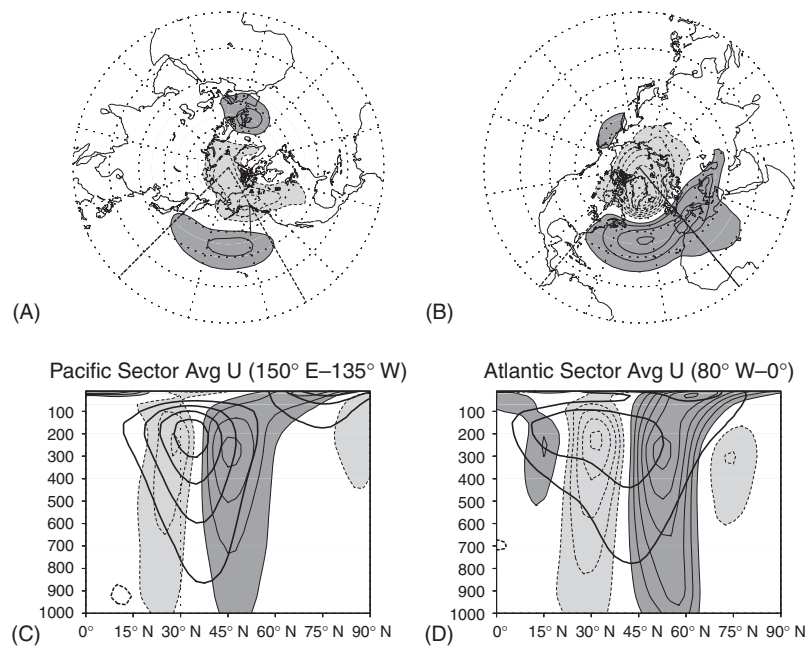
Figure 18 Comparison of the WP/NPO and NAO variability structures: sea-level pressure regressions are shown in panels A and B, with a 1.0 hPa interval. To facilitate comparison, maps are rotated so that both ocean basins are in the 6 o'clock position. Sector-averaged zonal wind regressions are shown in panels C and D with a 1.0 m s^{-1} interval, using thin shaded contours. Regressions are obtained in both cases using PCs from rotated analysis of 200 hPa height and SST anomalies during 1958–93 winter months. Superposed thick solid contours depict the climatological winter jet in the same sectors, with a 10 m s^{-1} interval. Sector definitions are based on the zonal extent of the subtropical high-pressure cell in panels A and B, and indicated by the solid meridian lines in those maps: 150° E–135° W in the Pacific and 80° W–0° in the Atlantic. The dark (light) shading in all panels denotes positive (negative) values in excess of the contouring interval. The zero contour is suppressed in the panels.

logical jet is weaker here and more diffused, the zonal wind anomalies are, latitudinally, just as coherent as the WP/NPO anomalies, and move the jet center poleward, as before. An additional feature present in NAO regressions is the weak zonal wind anomaly in the Tropics, which makes the already diffuse Atlantic jet even more so. The NAO zonal anomalies have comparatively stronger extensions into the stratosphere, but their structure *vis-à-vis* the local vortex is very similar, i.e., they too strengthen the local polar vortex. The jet perturbations are dynamically important, for they affect wave propagation, both in the troposphere, and between the troposphere and stratosphere. They can also be a wave source: by modulating flow over orography and over regions of strong climatological vorticity gradients. The dynamical and thermodynamical mechanisms connecting the troposphere and stratosphere during NAO variability is an area of active research.

Teleconnection evolution

Climate teleconnections, discussed above, were obtained from the analysis of *monthly* averaged anomalies, using techniques keyed to an optimal accounting of the temporal variance. These attributes steered the analysis towards extraction of the fully developed, or mature-phase, of the leading teleconnection patterns. Monthly-averaging was helpful in this regard for it filtered the large-scale synoptic waves in the troposphere, and facilitated focus on the 'standing' component of low-frequency variability. A month is not too long a period in context of large-scale ocean-atmosphere interaction, but it is a rather extended averaging period in the context of dynamical and thermodynamical processes operative in the generation of climate teleconnections. These processes evolve rapidly – on weekly time scales – and their resolution is critical for description of the nascent-to-mature phase evolution of teleconnection patterns, and for advancing understanding of the excitation mechanisms.

The typical evolution and longevity of the variability episodes associated with wintertime teleconnection patterns is investigated from analysis of the *weekly* (Sunday-to-Saturday) anomalies. The anomalies were constructed from the daily NCEP reanalysis and SST fields, by removing the weekly climatologies. The December–March winter season was defined to be 18 weeks long, with start dates falling between November 28 and December 4. Daily SSTs were however available only since November 1981, i.e., only for the

past two decades, which precluded a meaningful analysis of the combined SST and geopotential variability on weekly time scales. The ϕ_{200} anomalies were thus analyzed alone using the RPCA technique, but aliasing of ENSO variability was largely avoided by detrending the weekly data prior to the analysis: Height regressions against a *weekly* Nino3.4 SST index (constructed from linear interpolation of the monthly version) were removed from the weekly ϕ_{200} record. For consistency with monthly analysis, variability in the same 35 winter seasons (1958/59–92/93) is analyzed; the analysis domain and the number of PCs rotated are also the same as before. Analysis of weekly data also yields NAO (11.2%), and the WP (8.8%) and PNA (7.8%) patterns as the leading variability modes. (Note, ENSO variability is absent from the line-up as it was filtered from the weekly data record.)

The discussion of results obtained from weekly analysis is limited to an examination of PNA evolution, in the interest of space. The examination begins with an analysis of the longevity of PNA variability episodes. The auto-correlation statistic is used to estimate the pattern's duration; auto-correlation of the PNA PC is calculated at various weekly lead/lags in each winter season, and the 35-year mean and standard deviation is shown in **Figure 19**. The mean auto-correlation falls to ~ 0.5 within a week (and to e^{-1} within ~ 1.5 weeks) of attaining peak amplitude (the zero-lag phase). The typical duration of PNA episodes is thus 2-to-3 weeks, depending on the threshold criterion. Clearly, analysis of the sub-weekly averaged data (pentad averages, for example) can lead to further refinement of the duration estimate.

The structural evolution of PNA variability is examined next, again from the lead/lag regressions of its principal component. Regressions are generated, as before, for each of the 35 winters, and the mean regression structure is shown in **Figure 20** at various weekly lead/lags. Regressions of the upper-tropospheric rotational flow (ϕ_{200}) are shown in the left panels, while those of divergent flow (200 hPa divergence) are shown in the right panels. In both columns, time increases downward, with the peak PNA phase ($T = 0$ weeks) depicted in the middle panels.

The evolution of PNA height anomalies is interesting: A coherent signal is evident as far ahead as two weeks ($T = -2$ weeks); the precursor pattern contains hints of the extratropical features present in the mature phase, with the exception of the subtropical ridge in the central Pacific; the North Pacific trough deepens considerably, in advance of significant ridge development off the Hawaiian islands (cf. $T = -1$ week). These evolutionary features question the notion that the PNA pattern is generated by the
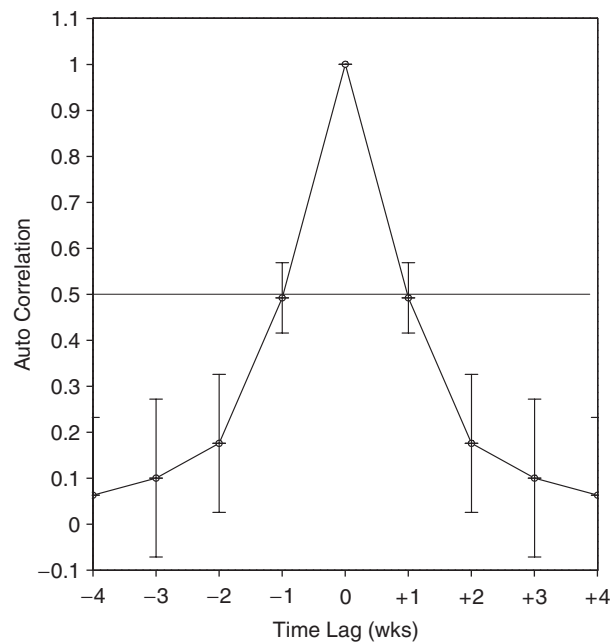
Figure 19 Duration of PNA episodes estimated from analysis of *weekly* 200 hPa height anomalies in 35 winters (December–March, 1958/59–92/93): Auto-correlation of the PNA principal component is calculated at various weekly lead/lags in each winter, and the 35-year means (solid line) and standard deviations (vertical bars) are displayed.

propagation of Rossby waves, emanating from the central tropical Pacific. The precursor patterns, in fact, exhibit interesting development in the extratropics. As geopotential height is related to the geostrophic wind, the precursor height features in the eastern hemisphere extratropics in the $T = -1$ and -2 week maps represent an eastward extension (and meridional tightening) of the climatological Asian-Pacific jet. Poleward and upward propagation of planetary waves (wavenumber 2, principally) into the lower stratosphere from the eastern extratropics (not shown) is also an interesting feature of PNA evolution.

The evolution of upper-tropospheric divergent flow in PNA episodes is also interesting, in that, the precursor phase is characterized by significant anomalies in the extratropics. The absence of significant upper-level divergence anomalies in the deep Tropics are notably absent, indicates a rather limited role of tropical convection, including the Madden-Julian oscillation, in initiating PNA variability. The mature-phase divergence anomalies have coherent, large-scale structure – a quadrupole – over the extratropical Pacific, with significant amplitudes over the central/eastern basin. Interestingly, the divergence anomalies are collocated with the upper-tropospheric diabatic heating anomalies (not shown). Such collocation is generally seen in the deep Tropics, but not in the
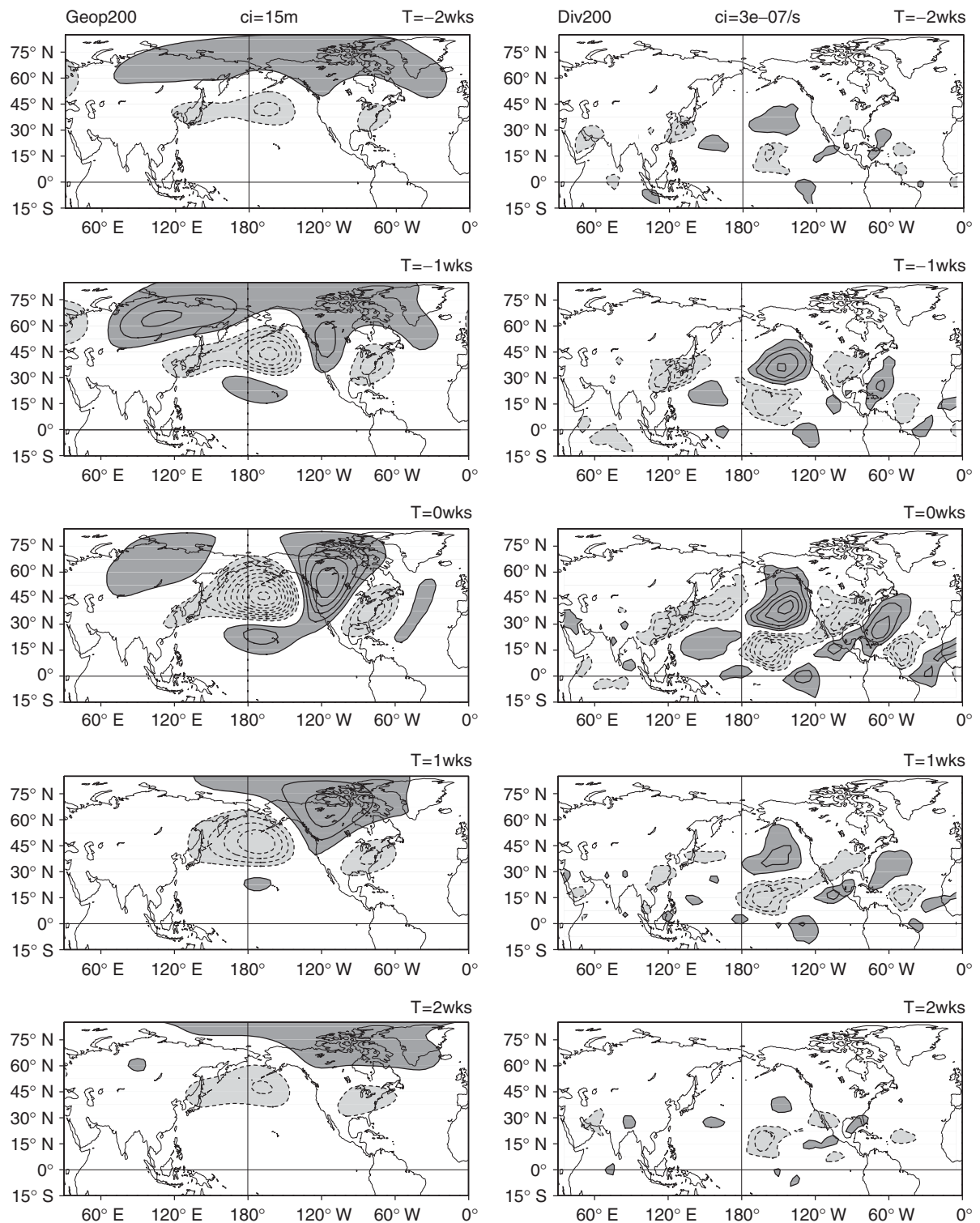
Figure 20 Weekly evolution of PNA variability: The 200 hPa height and divergence regressions of the PNA principal component are shown at various weekly lead/lags. The principal component was obtained from RPCA analysis of weekly 200 hPa height anomalies in 35 winters, after detrending the data for ENSO variability. Height regressions are shown in left panels using a 15 m contour interval, while the divergence ones are displayed in the right panels using a $3 \times 10^{-7} s^{-1}$ interval. Dark (light) shading denotes positive (negative) values in excess of the contouring interval. The zero contour is suppressed, as before, and time increases downward in intervals of a week. PNA's mature phase is depicted in the middle panels, and captioned $T = 0$ weeks.

extratropics. The collocation raises the possibility that divergence and heating anomalies are both generated by the same 'thermal-wind balance' restoring secondary circulations; the former, directly, while the latter, through their impact on Pacific stormtrack activity.

The evolution of surface winds and the underlying SST during PNA episodes is examined in **Figure 21**. The fields are of interest in view of the potential for air–sea interaction over the extratropical Pacific and its impact on PNA evolution. The mature phase structure was scrutinized earlier (cf. **Figure 2**) to glean the direction of interaction in the central/eastern basin, but that assessment needed corroboration from a more discriminating analysis. Weekly evolution of the 1000 hPa NCEP reanalysis winds is displayed in the left panels, while SST development is shown in the right panels of **Figure 21**. The SST analysis is based on regressions for the 12-winter sub-period (1981/82–92/93) during which daily SSTs are available. Examination of the antecedent structure reveals the presence of large-scale cyclonic circulation over the northern Pacific two weeks in advance of the mature phase (cf. $T = -2$ weeks); its initial extent is from the dateline to the North American coast, and, meridionally, from the Aleutian to the Hawaiian islands. Cyclonic development is quite rapid, for winds become several times stronger in a period of just one week (cf. $T = -1$ week). The cyclonic circulation is even stronger, fully extended across the midlatitude basin, and notably, more coherent along its western flank in the mature phase. The near-surface development largely tracks the upper-level evolution except for the westward shift with height of the precursor phase features.

The precursor SST anomalies are characterized by cold temperatures in the $30°–45°$ N Pacific band; anomalies appear to emanate from the Kuroshio exit region, off Japan, and extend eastward as far as $135°$ W. The cold band is surrounded by warmer temperatures in the eastern basin, with a bow-shaped pattern reminiscent of the structure of decadal variability; the warming is modest, though, with SST anomalies in the Gulf of Alaska and off Baja California ≤ 0.15 K. The role of precursor SST anomalies in generation of PNA variability is difficult to establish without more comprehensive analysis, including modeling. In contrast, the impact of evolving atmospheric circulation on SST is somewhat easier to characterize. Rapid development of cyclonic circulation in the northern basin leads to SST changes, which are comparatively modest, and which accrue slowly because of the thermal inertia of the oceanic mixed layer. Because of the lagged nature of the response, the cumulative changes in SST are shown both between $T = 0$ and $T = -2$ weeks, and $T = +2$ and $T = -2$ weeks. The similarity of cumulative changes with the mature phase SST pattern in the central/eastern basin is striking; approximately half of the mature-phase amplitude in these sectors is derived from SST development in the preceding two weeks. The structural similarity of PNA's mature phase SST patterns, as identified from monthly and weekly analysis (**Figures 13C** and **21**, respectively), is also noteworthy and reassuring.

The difference between the mature and precursor phase winds is shown in the bottom left panel of **Figure 21**. Anomalous surface westerlies over the open ocean enhance the wind speed in midlatitudes (by reinforcing the climatological westerlies) and diminish wind-speed in the subtropics (by opposing the climatological trade winds, which blow from the east). Sensible and latent heat fluxes at the ocean surface, and vertical mixing in the upper ocean are both sensitive to wind speed; increased speeds lead to greater fluxes and mixing, and consequently, colder SST. The cumulative changes in SST, depicted in the lower right panels, are consistent with this understanding: SSTs are cooler poleward of $\sim 30°$ N and warmer just to the south; the sweeping structure of warmer SSTs in the open ocean is consistent with the domain structure of the climatological trade winds. The wind direction can, additionally, be important near the coasts. Southerly anomalies along the eastern flank of cyclonic development are sufficiently near the coast to impact coastal upwelling. Southerly winds generate down-welling in the coastal zones of the Northern Hemisphere, and shield the upper-layers from the influence of colder sub-surface water. Thus, warming along the North American coast in the cumulative SST change maps can also be understood, reasonably, as resulting from the impact of the evolving near-surface winds.

To be sure, SST development must, in turn, influence aspects of concurrent PNA evolution, but culling this influence and estimating its importance is challenging without the benefits of a modeling analysis. Although, not directly indicative of the excitation mechanism, the precursor patterns in **Figures 20** and **21** allude to the importance of dynamical and thermodynamical interactions in the Northern extratropics in generation of PNA variability.

Investigation of teleconnection evolution using the lead/lag regression technique is not without its pitfalls, though, which include emphasis on structural similarity. Modal development can sometimes involve considerable evolution of spatial structure, as well. Shape-sensitive measures, like the ones used above, will be of limited value in these situations. The variability in such cases should be analyzed in the spatio-temporal domain using techniques, such as the extended EOF analysis, which simultaneously search for recurrence of both spatial and temporal patterns.
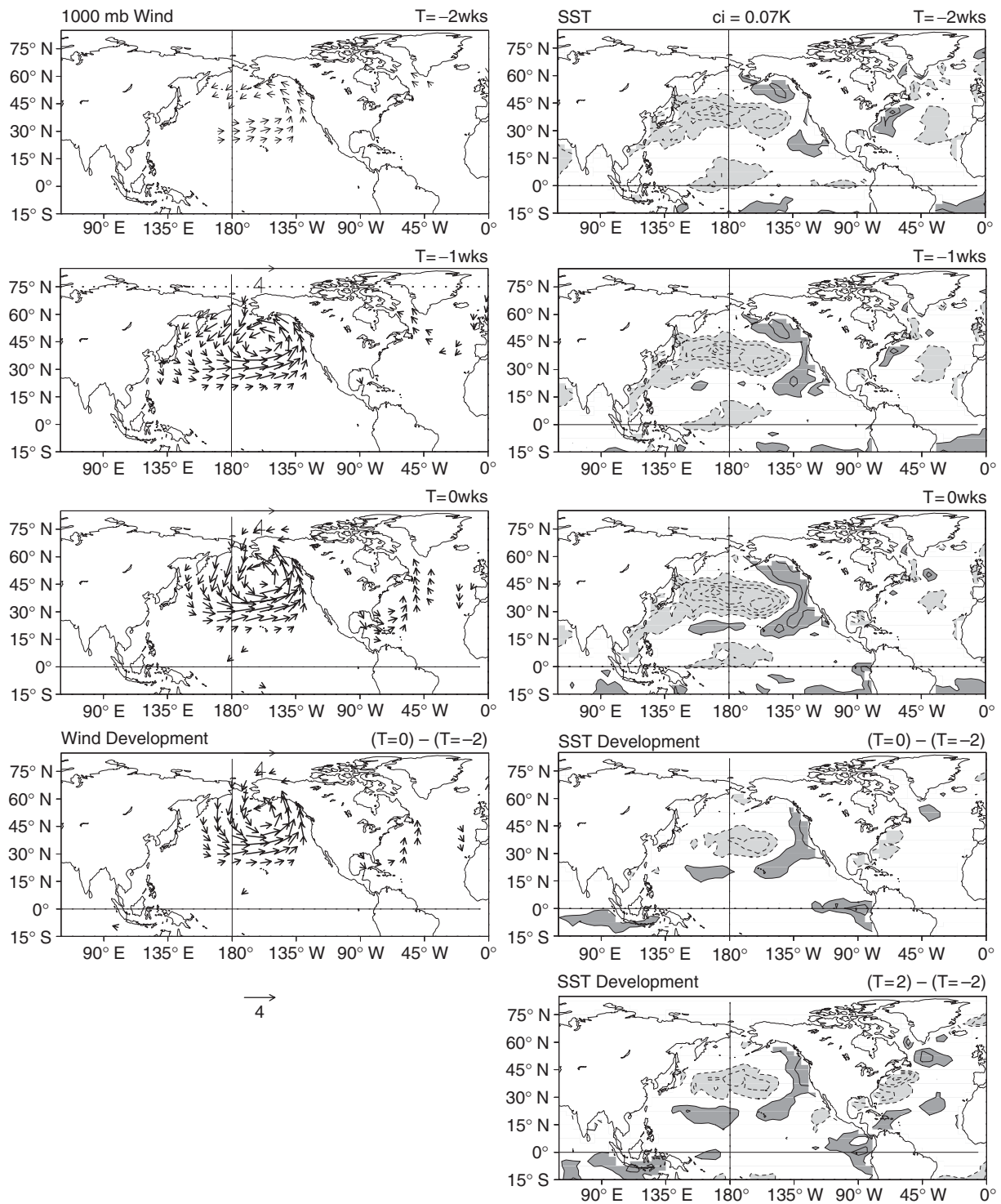
Figure 21 Weekly evolution of PNA variability: 1000 hPa winds and SST regressions of the PNA principal component are shown at various weekly lead/lags. The SST regressions are based on the 12-winter sub-period (1981/82–92/93) for which daily SSTs are available. Wind regressions are shown over oceanic regions in the left panels using the indicated vector scale, while SST regressions are displayed in the right panels using a 0.07 K interval. The shading convention is the same as in **Figure 20**. Time increases downward in intervals of a week. Wind and SST development (i.e., changes over a 2–4 week period) are displayed in the lower panels.

See also

Climate Variability: Seasonal to Interannual Variability. **Coriolis Force**. **Cyclogenesis**. **Dynamic Meteorology:** Overview; Waves. **Stationary Waves (Orographic and Thermally Forced)**. **Stratosphere–Troposphere Exchange:** Global Aspects.

Further Reading

James IN (1994) *Introduction to Circulating Atmospheres*. Cambridge: Cambridge University Press.

Wallace JM and Gutzler DS (1981) Teleconnections in the geopotential height field during the Northern Hemispere winter. *Monthly Weather Review* 109: 784–812.

THERMAL LOW

R H Johnson, Colorado State University, Fort Collins, CO, USA

Introduction

A thermal low (sometimes referred to as a heat low) is a low-pressure area resulting from high temperatures in the lower troposphere caused by a localized area of intense heating at the Earth's surface. Thermal lows occur typically during the summer over subtropical continental areas and are most intense in the desert regions of the world. These regions are characterized by clear skies and a lack of vegetation. Consequently, there is a large diurnal cycle of surface heating, which in turn creates a pronounced diurnal cycle in the intensity of thermal lows, with a maximum intensity (i.e., minimum surface pressure) during the afternoon. Because thermal lows are linked directly to surface properties, they are nonmigratory in nature. Moreover, they do not exhibit any frontal characteristics, nor are clouds or precipitation associated with them.

Since thermal lows arise from surface heating, the maximum amplitudes of temperature and circulation anomalies associated with them are confined to the lower troposphere (i.e., below 5 km or 500 hPa). Most of the desert areas of the world that exhibit strong thermal lows are surrounded by bodies of water. As a result, horizontal heating gradients that develop generate sea and land breezes that influence the thermal-low circulations. In regions away from the equator, the low-level inflow associated with the daytime sea breeze produces, through the action of the Earth's rotation (the Coriolis force), a cyclonic vorticity anomaly in the lower troposphere. The converging air at low levels in the thermal low also produces upward motion in the lower troposphere, but sinking motion occurs aloft. The cyclonic circulation often persists into the nighttime hours above the surface following the development of a shallow, nocturnal temperature inversion. By the morning, subsidence extends all the way down to the surface.

Because of the clear-sky conditions and high surface reflectance (albedo) of the desertlike areas where thermal lows persist, these regions have often been regarded as large-scale radiative energy sinks. However, in some thermal low regions dust is raised from the surface by the intense heating which results in short-wave absorption that makes at least a portion of the thermal low region a radiative energy source.

Geographical Distribution

The strongest thermal lows are located over the great deserts of the world, e.g., the Sahara, Arabian, Kalahari, Australian Great Western Desert, and Mojave/Sonoran Deserts. In these regions the thermal lows are so strong that they appear as closed lows or troughs in the mean-sea-level pressure maps of the summer hemispheres (**Figure 1**). For example, note the low-pressure troughs over the African Sahara, the Indian subcontinent, and the Southwest US in July and over northern Australia in January. The trough over southern Asia near India in July is closely associated with cross-equatorial flow over the western Indian Ocean and the Asian summer monsoon.

The locations of thermal lows also correspond to regions of intense surface heating, as can be seen from a map of the global distribution of surface sensible heat flux (**Figure 2**). The lack of cloudiness, vegetation, and surface moisture in these regions accounts for the large values of surface sensible heat flux. Maximum values upwards of 60–70 W m^{-2} can be seen in the regions of the major deserts. The close relationship between the thermal lows and surface sensible heat flux patterns indicates a close physical linkage between these two features. Specifically, intense, localized heating warms the lower atmosphere and hydrostatically reduces the surface pressure in that region.

The wind vectors illustrated in **Figure 1** show generally confluent surface flow into the thermal low-pressure areas. This flow arises from strong horizontal gradients in the surface sensible heat flux between the desert areas and the surrounding oceans